



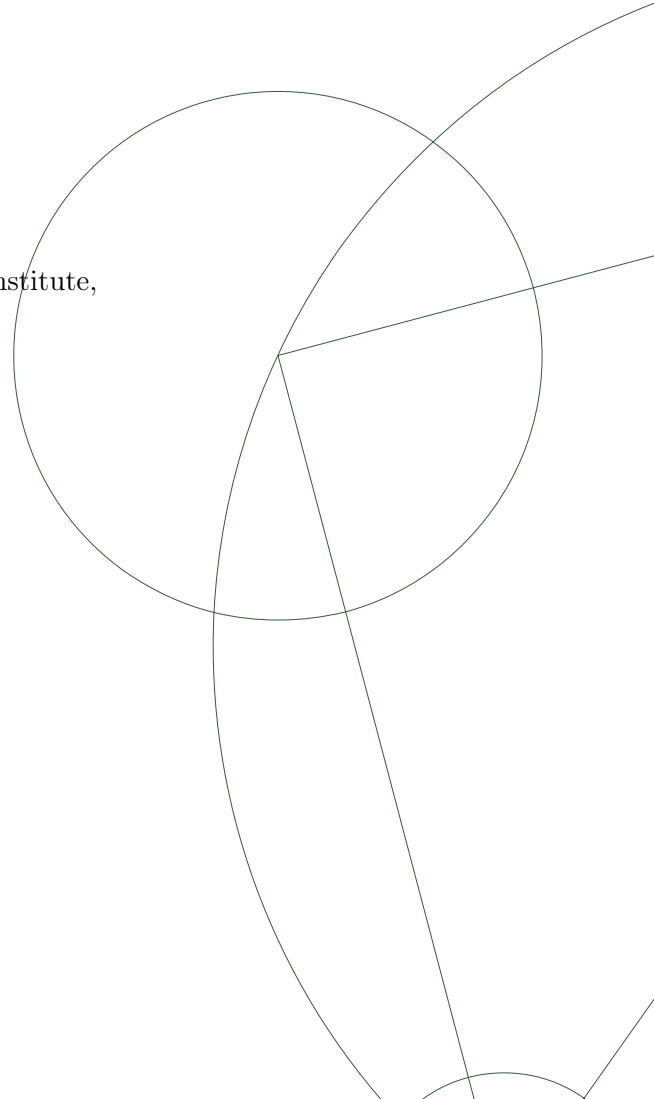
An attempt of obtaining a chronologically correct reconstruction of the NEEM disturbed section

Luca Foresta

Supervisors:

Peter Ditlevsen, Peter Langen,
Centre for Ice and Climate, Niels Bohr Institute,
University of Copenhagen

Niels Bohr Institute
University of Copenhagen
December 20th, 2011



Contents

1	Introduction	11
2	Framework	13
2.1	Climate Archives	13
2.2	Ice cores	16
2.3	Deep drilling in Greenland: a brief overview	21
2.4	Disturbed Eemian ice	26
2.5	Tentative reconstruction of the last interglacial	30
3	The method	33
3.1	Generation of candidate solutions	35
3.2	The match function	39
3.3	Test	54
4	The reference profile	59
4.1	A Greenland profile of the Eemian	59
5	Results	70
5.1	Semi-automatic match between NEEM unfolded section to NGRIP	70
5.2	NGRIP: synthetic folded data	73
5.3	Corrupted sections of ice at NEEM and Summit	80
6	Conclusions and discussions	92

List of Figures

2.1	Sketch showing the vertical thinning and horizontal stretch of the layers (green). The black arrows indicate the flow directions, opposite respect to the ice divide (orange line). Source: <i>Centre for Ice and Climate</i> . 17	17
2.2	(a) Archives best sampling resolution dt plotted versus their temporal range \mathcal{T} (data according to table 2.1). The perfect record would lie on the bottom right with infinite \mathcal{T} and infinitesimal dt . (b) Ratio \mathcal{T}/dt per climate archive. 19	19
2.3	Illustrative picture of air masses moving poleward and being depleted in heavy isotopes by selective precipitation. Numbers refer to δD . (Source: <i>Centre for Ice and Climate</i>) 21	21
2.4	Map of Greenland. Coordinates: GISP2 (72.36° N - 38.30° W), GRIP (72.35° N - 37.4° W), NGRIP (75.1° N - 42.32° W) and NEEM (77.45° N 51.06° W) (NGRIPmembers et al. (2004) modified; originally provided by S. Ekholm, Danish Cadastre).) 22	22
2.5	GISP2 and GRIP $\delta^{18}O$ versus depth. Resolution is 2m and 2.2m respectively, based on 1m and 0.55m data sets. Highlighted in red the mismatching part. After Grootes et al. (1993), modified. 23	23
2.6	NorthGRIP shown on the GICC05modelext time scale (Vinther et al., 2006; Rasmussen et al., 2006; Andersen et al., 2006; Svensson et al., 2008; Wolff et al., 2010). 25	25
2.7	Unpublished data (members). 26	26

2.8	Radio echo sounding surveys at (a) NGRIP and (b) GRIP. The bed topography is clearly different in the two cases (Nixdorf and Goktas, 2001).	28
2.9	Ground penetrating radar (GPR) survey at Fletcher Promontory ice cap (Antarctica) showing a Raymond arch under the ice divide (not visible here). After Vaughan et al. (1999)	29
2.10	The deformation of a disturbed layer under (a) pure shear and (b) simple shear. Pure shear, with vertical compression, flattens the disturbance. Simple shear steepens (and overturns) the A-B limb while leaving the disturbance amplitude unchanged. After Jacobson and Waddington (2004)	30
2.11	Greenland $\delta^{18}\text{O}_{\text{ice}}$ (temperature proxy) compared to Vostok temperature. Also shown are CO ₂ , the reconstructed Greenland methane record, the reconstructed $\delta^{18}\text{O}_{\text{atm}}$ record, $\delta^{15}\text{N}$ of N ₂ , and $^{17}\Delta$ of O ₂ . Shaded circles and solid triangles are the measurements of the disturbed section of the GISP2 core and the GRIP core, respectively, plotted versus best estimate ages. (a) Between 160 ka and 100 ka and (b) between 250 ka and 200 ka. The $\delta^{18}\text{O}_{\text{ice}}$ of planktonic foraminifera from the Iberian margin (MD952042) is also plotted for Figure 9a. After Suwa et al. (2006).	31
3.1	Sketch of a recumbent folding. An ice core drilled through this feature would retrieve the layers A-B-C at least twice; the second section is inverted in depth.	35
3.2	Amount of configurations generated by <i>Operations</i>	39
3.3	Cascade of configurations generated by <i>Operations</i> when n=3.	40

3.4 Four-dimensional search strategy. (a) A circular template from the center of the reference image is cropped. (b) For every position in the target image, a circular region is selected and compared against the circular template in (a) to find the best (T_x, T_y) . (c) Search for (R, S) in the log-polar domain. After Zokai and Wolberg (2005), fig 7. 41

3.5 (a) Observed images: 4 zoom, arbitrary rotation, and moderate perspective. (b) Registration results highlighted on reference images. After Zokai and Wolberg (2005), fig 8 (selection). 43

3.6 Steps (1-3) of table 3.4 for two synthetic functions y_1 and y_2 , where the latter is a rescaled and translated version of the former. The second step is split in (a) bottom and (b). 47

3.7 Pairs of synthetic profiles f_1-f_2 (blue) and g_1-g_2 (red) with uniform sampling in the Cartesian (a) and logarithmic (b) space, respectively. The pivot of the transformation is x_0 (black dot, left panel). Functions f_2 and g_2 are rescaled versions of f_1 and g_1 50

3.8 Scale factor search with uniform grid in the Cartesian (blue) and logarithmic (red) space. Dots represent discrete samplings in the two spaces. The best choice for each case is highlighted. The shaded lines are running means of the infinitely refined samplings (thin lines). The trough is broader in the log space and therefore more easily detected. 51

3.9 Three cycles of refinement are shown. The initial grid (black) has $N \times S = 6 \times 7$ elements. The neighbourhoods' sizes are set to $\kappa = 2$ and $\sigma = 1$, around (dx^*, s^*) (red dot). The new grid (green) is formed by this area, filled with $p = 2$ and $q = 3$ new elements along the \mathcal{N} and \mathcal{S} dimensions, respectively. The whole process runs once more producing the blue grid. Note that the points of the previous grid, which are inside the neighbourhoods, are conserved throughout the cycles (black dots in the green grid; black and green dots in the blue grid). 53

3.10	Example of a mismatch when the \mathcal{N} vector is poorly defined. The upper panel shows NGRIP $\delta^{18}\text{O}$ profile (blue) and a selection of it: DO 19-21 (red). The lower panel shows the mismatch setting $N=50$ in <i>Match</i>	55
3.11	Simple test performed on the <i>Match</i> algorithm in order to check its reliability. A section of the NGRIP record (blue) is translated and rescaled (red, upper panel). The output of the routine is shown in the lower panel.	57
3.12	Video showing how the <i>Match</i> algorithm works. Details in the text.	58
4.1	Schematic of the thermal bipolar seesaw model. The original BS is coupled to a heat reservoir representing the Southern Ocean. After Stocker and Johnsen (2003).	61
4.2	Synthetic reconstruction of Greenland temperature variability (GL_T -syn, red curve) compared to GISP2 $\delta^{18}\text{O}$ profile (GL_T , green curve) tuned to EDC3 via methane. Numbers identify the Dansgaard-Oeschger events. After Barker et al. (2011).	63
4.3	Comparison between Barker et al. (2011) synthetic Greenland profile (green) and reconstruction of their method (blue). Each curve on its time scale (see details in the text).	64
4.4	Detailed view of the first ~ 140 Kyr of the two profiles in fig 4.3.	65
4.5	(Top panel) Comparison between the NGRIP record versus the original depth (blue line) and the equivalent depth (green). (Bottom panel) Same for the EDC record.	66
4.6	Reconstruction from Barker and colleagues cropped at ~ 140 Kr BP converted to equivalent depth (green line). Also shown the NGRIP profile versus its original depth. The red dot indicates the merging point (see text in the next section).	67

4.7 Combined reconstruction of the $\delta^{18}\text{O}$ profile during the Eemian period. The red dot indicates the merging point between the NGRIP data (left) and the GL_T reconstruction (right). 68

5.1 Semi-automatic match between NGRIP (blue) and NEEM (green) $\delta^{18}\text{O}$ data series. The NGRIP profile is divided into five sections. The vertical black lines identify the initial value of each section. The scale and translation factors applied to the intervals are given in table 5.1. Specifics of *Match* are: $\text{NxS}=150 \times 50$; $\mathcal{S}=[.2, 2]$ 71

5.2 Generation of a corrupted version of the NGRIP $\delta^{18}\text{O}$ profile (blue line). The first interval is copied and reversed, the last two are interchanged. Moreover, an arbitrary scale factor is applied on the folded signal. 74

5.3 (Top panel) The original NGRIP profile (blue) is broken into four intervals I_k by the application of three breakpoints (black dots and lines). (Bottom panel) Disturbed NGRIP version (green) constructed by (1) the removal of I_1 , (2) the reversal of I_3 and (3) the swap of I_2 with I_3 . At last, (4) an arbitrary factor is applied on the green profile. The *Main* program is run several times, setting the breakpoint and increasing distance from the original positions (red dots). The shift is randomly positive or negative. The results of the simulations are given in fig 5.5. 76

5.4 Minima of the 78 comparisons performed by the *Main* program for the first simulation (black breakpoints in fig 5.3 lower panel). The three panels cluster the configurations generated using only one interval (left), two intervals (center) or all (right). A black circle indicates the absolute minimum in each group. 77

5.5 Results from the seven *Main* runs corresponding to different choices of the breakpoints in fig 5.3 bottom panel. From 0 to 6, the position's offset is iteratively increased by 1 Kyr (see 5.3 zoomed boxes). 79

5.6	NEEM record. The disturbed section is shown in the upper panel. Only a specific range is selected for the simulations. Below $\sim 2430\text{m}$ depth, the ice is assumed to be older with respect to the Eemian period.	82
5.7	Alignments of the three intervals selected in the disturbed NEEM section. Both orientations are shown. In panel (c), two shades of green are used to better visualize the superposing lines.	84
5.8	GISP2 record. The disturbed section is shown in the upper panel. The cyan blue line indicates the sections of ice not used in the simulation.	86
5.9	Alignments of the three intervals selected in the disturbed GISP2 section. Both orientations are shown.	87
5.10	GRIP record. The disturbed section is shown in the upper panel. Only a specific range is selected for the simulations. Data below $\sim 2780\text{m}$ depth were not included in the simulations. The cyan blue line indicates the sections of ice not used in the simulation.	90
5.11	Alignments of the six intervals selected in the disturbed GRIP section. Both orientations are shown.	91

List of Tables

2.1	Examples of climate archives, together with their minimum sampling interval, temporal range covered and the list of information potentially provided. After Bradley (1999).	15
3.1	Configurations generated by the <i>Copy</i> (a), <i>Reverse</i> (b) and <i>Interchange</i> (c) operators when applied separately to a function divided into three intervals (n=3). Intervals have Roman enumeration (columns). Rows are configurations. Respectively, $\Pi_c=2^3-1=7$; $\Pi_r=2^3=8$; $\Pi_i=3!=6$. 37	37
3.2	Example of generation of identical configurations. (a) <i>Interchange</i> is applied to a function divided into n=3 intervals. (b) Interval III is erased (part of <i>Copy</i>), producing three couples of identical combinations (b-c).	38
3.3	LPT algorithm from Zokai and Wolberg (2005). The procedure is applied recursively from coarse to fine resolution.	42
3.4	Logical steps of the cycles	47
3.5	Robustness of the algorithm's output. The rows are different matches, performed with one cycle and N=200. The first two columns are the boundary values of y_2 ; the third and fourth are the scale and translation values which best align y_2 to y_1	56

5.1	Initial and final x values (first and second columns) of the five NGRIP sections (rows) matched to the NEEM $\delta^{18}\text{O}$ profile. The scale and translation factors applied to each section are listed in the third and fourth columns.	72
5.2	NEEM. Boundaries (first two columns) of the selected intervals. The scaling and translation are given respectively in the third and fourth columns for both possible orientations (shown by the arrows).	81
5.3	GISP2. Boundaries (first two columns) of the selected intervals.	85
5.4	GRIP. Boundaries (first two columns) of the selected intervals.	88

Chapter 1

Introduction

The work in this thesis is focused on the deepest section of the NEEM (North Greenland Eemian Ice Drilling) ice core, whose site is located in North-West Greenland (77.45°N - 51.06°W). This international deep ice core project was specifically aimed at retrieving ice spanning the entire previous interglacial period: the Eemian or MIS-5 (Marine Isotope Stage 5).

Such period is highly interesting because the temperature was $\sim 5^{\circ}\text{C}$ higher with respect to present conditions and models estimate a temperature rise of 2-6°C by the end of the century (NGRIPmembers et al., 2004; IPCC, 2007). Therefore, knowledge about the Eemian period evolution would give insight into the possible next future of the Earth climate.

Drilling activities ended in 2010 when bedrock was reached at 2537.36m depth. The last section of the core contains clear evidence of "warm" ice characterized by high $\delta^{18}\text{O}$ values, far above the average level of the younger glacial ice. Nevertheless, below $\sim 2200\text{m}$ depth, the stratigraphy appeared to be corrupted, as it was at Summit (GISP2 and GRIP ice cores, Greenland).

The aim of this work is to investigate the possibility to obtain a chronologically consistent representation of the deepest part of the NEEM ice core. The framework

of the thesis is given in chapter 2. At first, climate archives are introduced; more insight is given to ice cores, due to the central role of such records in this work. Subsequently, after a brief survey of the deep drilling projects in Greenland, possible reasons for the ice layers' disturbances are investigated. At last, previous works focused on the deepest data series at GISP2 and GRIP are summarized.

Chapter 3 is the core of the thesis and describe in details the different routines developed. Considerable space is given to the *Match* algorithm, which can be used independently from the rest of the program. In fact, given two any functions (not necessarily ice core data), such algorithm estimates the translation and scale factors which best align them.

The results are shown in chapter 5. This section is divided into three parts. (1) Results using only the *Match* algorithm, (2) the output of the program on synthetic corrupted data and (3) application of the general method on the NEEM disturbed section. Moreover, given the generality of the approach, a tentative application was performed on GISP2 and GRIP records as well.

Since the method is based on comparisons, a reference profile of the Eemian period had to be generated before applying the whole program to the three records. This process, based on the inverse thermal bipolar seesaw model, is described in chapter 4.

The author wishes to thank the whole NEEM community and the team at the Centre for Ice and Climate at the University of Copenhagen for providing the NEEM data, still unpublished, and allowing their use for this MSc thesis.

Chapter 2

Framework

2.1 Climate Archives

The climate system is defined by the Intergovernmental Panel on Climate Change (IPCC) as a complex interactive system formed by five domains: atmosphere, biosphere, cryosphere, hydrosphere and land surface. These domains interact together in a complicated manner determining the time evolution of the system according to the internal dynamics and external processes such as solar variations or human-induced forcings (IPCC, 2007).

In the last decades, the study of the Earth's climate has received increasing attention and resources. One of the main reasons for this growth of interest was most likely the question whether climate was changing and if mankind may had a role in its causes. Only 21 years ago the IPCC published the FAR (First Assessment Report, 1990). Three more were to follow at about five years intervals: SAR (1995), TAR (2001) and AR4 (2007). And AR5 is currently a work in progress with about eight hundreds authors involved. Each of these assessments is composed of specific reports, focusing on the different aspects of the topic. Climate change, in fact, is not only a scientific matter: it has environmental, sociological and economical impacts as well. Therefore, as climate change effects are not only of mere academic interest,

but are in fact a concern of everybody, this debate stimulated research and efforts towards an improved knowledge of the processes which characterize the climate system. Insight in its natural variability is essential in order to address climate change amplitude and patterns as well as quantify human contribution. For this purpose, past climate states on every possible time scales must be investigated.

Paleoclimatology is the branch of science dealing with such task. By definition, the period of study covers Earth's history prior to modern time, when the introduction of satellite and ground instrumental measurements allowed for closely tracing weather trends. In order to reconstruct previous planetary conditions, climate archives need to be investigated.

In general, an archive is a collection of past documents of some kind, available at any time in the future. A climate archive, specifically, is a proxy which stores information about physical, chemical, geological, and biological records. It is a window to the past, where researchers can look into and reveal previous conditions of the Earth, e.g. its atmospheric composition, sea-ice extent or vegetation cover, on both regional and global scales.

Climate reconstructions can be inferred by the use of these archives. The obtained data profiles will depend on their properties, such as the time range covered by and the finer temporal resolution visible in the records. Moreover, different informations are preserved and potentially provided in the different cases, as well as their continuity throughout the period spanned.

Depending on the kind, the proxy is usually associated with either the growth (e.g. tree rings, corals) or deposition process (e.g. sediments, ice cores). An interesting exception are insects' fossils: in this case the key process is migration. It is an accepted assumption that insects maintained the same ecological requirements through time (Bradley, 1999). Therefore, stenothermic species, i.e. sensible to a narrow range of temperature, respond to abrupt changes by migrating to another region with conditions more suitable for their needs. Being their exoskeleton well preserved in some

Archive	Minimum sampling interval	Temporal range (yr)	Potential information provided
Historical records	day/yr	$\sim 10^3$	T-P-B-V-M-L-S
Tree rings	yr/season	$\sim 10^4$	T-P-B-V-M-S
Lake sediments	yr (varves) to 20yr	$\sim 10^4$ - 10^6	T-P-B- C_w -M-V
Corals	yr	$\sim 10^4$	T-P- C_w -L
Ice cores	yr	$\sim 5 \times 10^5$	T-P- C_a -B-V-M-S
Pollen	20yr	$\sim 10^5$	T-P-B
Speleothems	100yr	$\sim 5 \times 10^5$	T-P- C_w
Paleosols	100yr	$\sim 10^6$	T-P-B
Loess	100yr	$\sim 10^6$	P-B-M
Geomorphic features	100yr	$\sim 10^6$	T-P-V-L
Marine sediments	100yr	$\sim 10^6$	T-P- C_w -B-M-L

T = temperature

P = precipitation

C = chemical composition of air (C_a) or water (C_w)

B = information on biomass and vegetation pattern

V = volcanic eruptions

M = geomagnetic field variations

L = sea level

S = solar activity

Table 2.1: Examples of climate archives, together with their minimum sampling interval, temporal range covered and the list of information potentially provided. After Bradley (1999).

environments (e.g. lakustrine sediments), the species can be identified with precision and insect-based climate reconstructions can be inferred by comparison with nowadays' conditions of sites hosting similar insects' clusters.

Other biologic archives like tree rings or corals, instead, show seasonal variability associated with different growth rates in response to a change in temperature at the site. In the former case, wider low density rings and thinner high density rings alternate when the warm season changes to winter condition. On the other hand, corals fastest growth, producing high density strata in the record, is associated with periods of highest sea surface temperatures (SST).

Some historical documents describing exceptional conditions of the climate exist, too. For example, 1816 is often called *The Year Without a Summer* as the north-eastern U.S. and Europe experienced a severe drop in temperature, probably due to an unfortunate combination of extremely low solar activity (the Dalton minimum) and the greatest volcanic eruption since Roman times (Stothers, 1984). This extreme phenomenon is documented in several articles and diaries published at the time and in the years to follow. However, even if providing some insight in local conditions of the climate, such documents provide limited information concerning the whole span of Earth's history.

2.2 Ice cores

The work in this thesis is focused on a specific type of climate archive: ice cores. The basic process involved in such archives is deposition. In areas characterized by the absence of melting and sublimation, the *dry-snow* zone (Benson, 1961), a new layer of snow accumulates every year. Embedded in each annual increment are gases and impurities characterizing the atmosphere in the air column above the surface. In time, the layers are both thinned and stretched. Thinning results along the vertical dimension because of increasing pressure due to the new precipitation; horizontal stretch is a consequence of the ice flow pattern. A sketch is given in fig 2.1. Any

core drilled aside from the ice divide, i.e. the line separating the directions of the flow (orange vertical line in fig 2.1), will contain ice originally deposited up-stream.

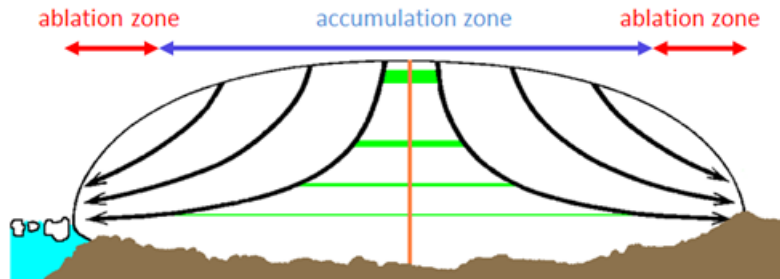


Figure 2.1: Sketch showing the vertical thinning and horizontal stretch of the layers (green). The black arrows indicate the flow directions, opposite respect to the ice divide (orange line). Source: *Centre for Ice and Climate*.

Drilling an ice core in the dry-snow zone reveals older strata with increasing depth. Therefore, a fundamental requirement in all accumulation-based proxies is the record to have preserved unaltered the history of deposition through time. This is most important, because if layers-corrupting processes are in place, information retrieved from the ice will be of very limited use. It would be still very interesting to know, e.g., that back in time Greenland experienced particularly cold conditions. However, without being able to place this cold event in a time frame, all information about causes generating and effects produced by this event would remain unknown. Moreover, the possibility of inferring predictions from similar conditions would be prevented.

Ice records can be divided in shallow and deep cores, drilled either in mountain glaciers or continental ice sheets such as in Greenland and Antarctica. Typical lengths vary from a few tens (shallow core) to a few hundreds (mountain glacier core) to ~ 3 thousands meters for a deep drilling project on a continental ice sheet. In principle, the longer the core the older will be the ice at the bottom given the absence of melting or sublimation processes and assuming no corruptions due to ice

flow disturbances. However some processes, e.g. the precipitation rate, influence the time window spanned by the record and its temporal resolution. In Greenland, where the accumulation is typically higher than Antarctica, more abundant precipitation is deposited each year, thus resulting in a shorter time domain but with finer temporal resolution. In fact, the thicker the strata in the core, the easier is to detect them, e.g. by visual stratigraphy.

From table 2.1 it is visible that these records are among the most powerful tools to investigate past climate conditions of the Earth; fig 2.2 is constructed from this table. Each climate record¹ is represented as a dot whose coordinates are the time domain \mathcal{T} (x axis) and minimum time resolution available dt (y axis); the size of the dots represents qualitatively the amount of potential information provided by the record. The ideal combination would lie on the bottom right of the (\mathcal{T}, dt) plane, with infinite \mathcal{T} and infinitesimal dt . Above the records reaching about one million years before present or more, ice cores (blue dot) have by far the best possible resolution. Another way to see this is to plot the ratio \mathcal{T}/dt for each archive. This number states the time sampling of the record in the ideal situation that the best time interval can be applied on the whole record. It is a qualitative measure of weighting the time domain by its best resolution. According to table 2.1, the best ratio $r_{best} = \mathcal{T}_{max}/dt_{min}$ would be 10^7 . The ratio closer to r_{best} will be the archive with the best combination of factors. Clearly, fig 2.2b shows that ice cores represent the best combination in terms of temporal range covered and minimum sample resolution².

Furthermore, fig 2.2 highlights that ice cores store a wide range of climatic variables (dot size) and can therefore give insight into the Earth's system on both regional and global scales. Analyses of the samples typically include:

- stable isotopes of water

¹Historical records are not included here

²It is worth noting that in Greenland, a resolution as fine as sub-annual at $\sim 2000\text{m}$ depth (~ 38 Ka BP) has been achieved (Thomas et al., 2009).

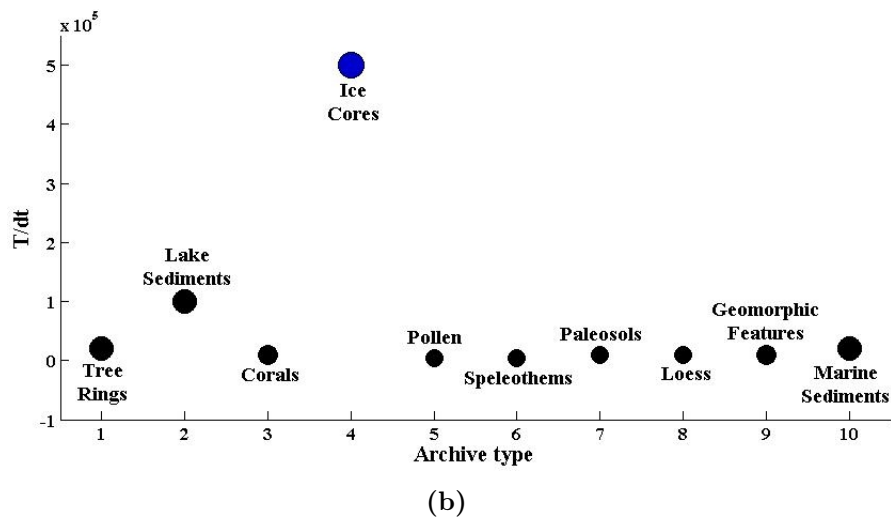
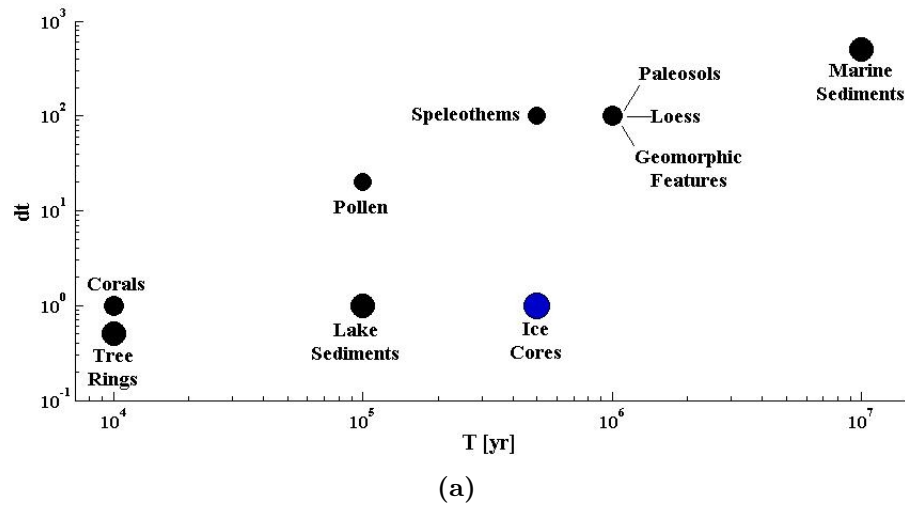


Figure 2.2: (a) Archives best sampling resolution dt plotted versus their temporal range \mathcal{T} (data according to table 2.1). The perfect record would lie on the bottom right with infinite \mathcal{T} and infinitesimal dt . (b) Ratio \mathcal{T}/dt per climate archive.

- visual stratigraphy
- acidity
- gases in air bubbles trapped in the ice
- impurities
- crystal structure of the ice

A detailed list of all the different measurements performed on and the types of information potentially provided by an ice core record is beyond the scope of this thesis. Nonetheless, since the data used in this work are stable isotopes profiles, a description of the processes involved is outlined in the following section.

Stable isotopes in ice cores' studies

Water molecules are formed by two hydrogen atoms and one oxygen atom; the former has two stable isotopes (^1H , ^2H or D), the latter three (^{16}O , ^{17}O , ^{18}O). Therefore the H_2O chemical compound, unable to distinguish between different isotopes, can be formed in nine different combinations. Two of them, HDO ($^1\text{H}^2\text{H}^{16}\text{O}$) and $^1\text{H}_2^{18}\text{O}$, are important in paleoclimatic studies because they have lower vapor pressure than the more common H_2^{16}O . Thus, they respond to a temperature drop condensing more easily. This is at the basis of the fractionation process. As humid air masses are advected poleward, they condense because of the temperature drop, producing precipitation enriched in heavy isotopes, whose response to a temperature change is faster.

The bigger the change in T, the lower the final concentration of the heavy isotopes respect to the original water parcel. As a consequence of that, snow accumulating in Greenland has lower concentrations of heavy isotopes with respect to low latitudes throughout the year and the lowest values in winter when temperature reaches the yearly minimum. This process is pictured in fig 2.3.

Thus, stable isotopes are a proxy for the local temperature at the site's surface.

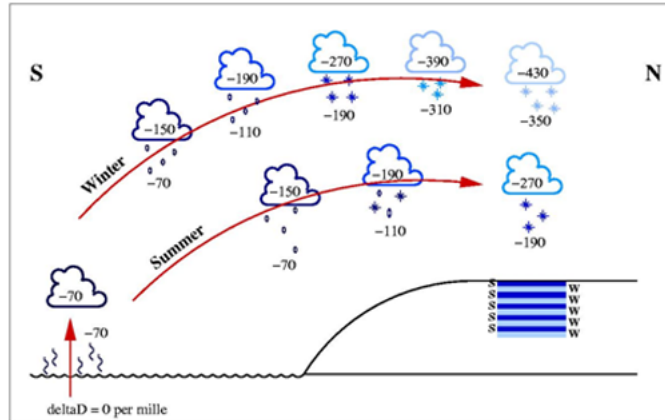


Figure 2.3: Illustrative picture of air masses moving poleward and being depleted in heavy isotopes by selective precipitation. Numbers refer to δD . (Source: *Centre for Ice and Climate*)

Several studies have found that in polar regions a quite simple relation exists between the two fields (e.g. Jouzel et al. (1994)):

$$\delta^{18}O = \alpha T + \beta \quad . \quad (2.1)$$

where α and β are constant coefficients. The δ notation expresses the departure of the ratio $r = [^{18}O] / [^{16}O]$ from a given standard. In the case of oxygen:

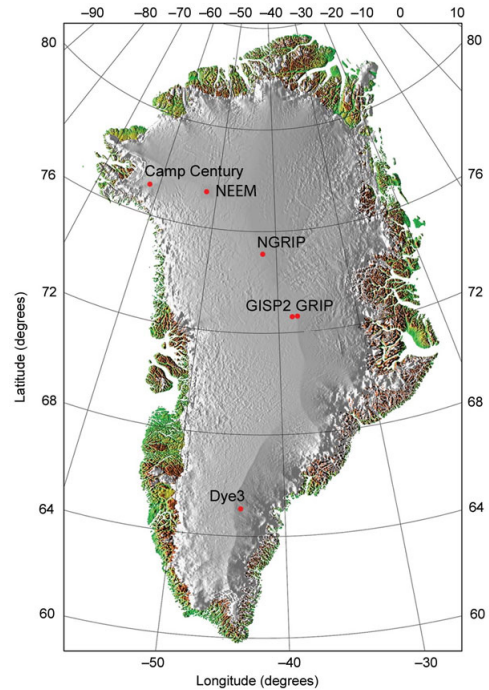
$$\delta^{18}O = \frac{r_s - r_{std}}{r_{std}} \cdot 10^3 \text{‰} \quad (2.2)$$

where s and std denote the sample and the standard respectively.

2.3 Deep drilling in Greenland: a brief overview

It was 1966 when, for the first time in history, an ice core was drilled down to the bedrock of an ice cap at $\sim 1390\text{m}$ depth. The site was Camp Century, formerly an American subsurface military base located in the north-west of the Greenland ice sheet. The record extended into the last glacial revealing fast and abrupt transitions

Figure 2.4: Map of Greenland. Coordinates: GISP2 (72.36° N - 38.30° W), GRIP (72.35° N - 37.4° W), NGRIP (75.1° N - 42.32° W) and NEEM (77.45° N 51.06° W) (NGRIP-members et al. (2004) modified; originally provided by S. Ekholm, Danish Cadastre).)



from cold stadial to warmer interstadial conditions.

Such a high variability pattern was not expected and had to be confirmed or confuted. For this reason, in the 1970s, shallow to intermediate records were drilled at different locations under the Greenland Ice Sheet Program (GISP), established in 1972. The efforts of this project culminated in 1981 in a $\sim 2000\text{m}$ deep core: DYE3. Analysis of these samples supported the previous result from Camp Century that the climate of the last glacial period was dominated by sharp temperature variations of large amplitudes, at least on a regional scale around Greenland.

DYE3 was the last effort under the GISP consortium and marked the end of the first period of ice coring in Greenland. The technical challenge of deep drilling in extreme conditions had been successfully tested, and ice records confirmed to be a promising archive of information about Earth's climate history.

These results led the way in the late 1980s towards two new parallel deep drilling projects: GISP2 and GRIP (GREENland Icecore Project), respectively American and European. The new site was carefully chosen in order to maximize the length of

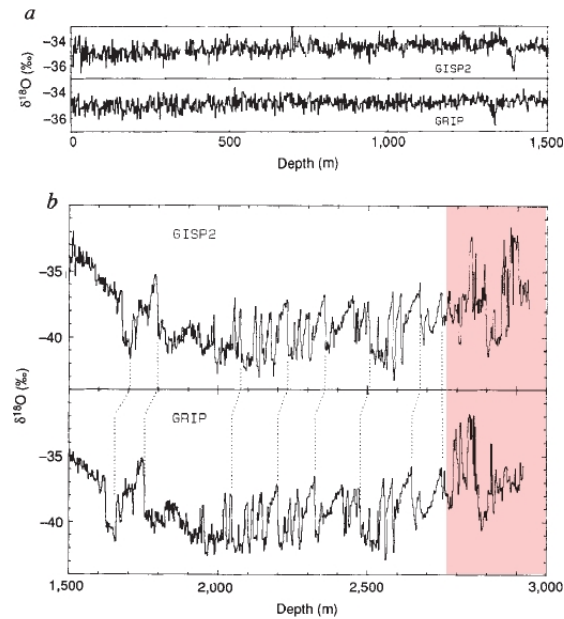


Figure 2.5: GISP2 and GRIP $\delta^{18}\text{O}$ versus depth. Resolution is 2m and 2.2m respectively, based on 1m and 0.55m data sets. Highlighted in red the mismatching part. After Grootes et al. (1993), modified.

the ice record and to minimize ice flow effects. This criterion should in principle permit to achieve climatic information on a longer time scale, without the need for introducing corrections for the ice flow.

The GRIP core was drilled on the very summit of the Greenland ice sheet (Summit) and GISP2 was positioned about 30 km west of the ice-divide. The two cores, respectively 3029 and 3053 meters deep, provided a coupled record of the history of the whole last glacial period, back to the previous interglacial and possibly further back in time (GRIPmembers et al., 1993; Grootes et al., 1993).

The almost perfect match between the two records for as much as 90% of the length of the cores (Grootes et al., 1993) validated with no further doubts the picture arisen from previous deep ice core stable isotopes profiles. In fig 2.5, it is possible to appreciate their similarity down to $\sim 2750\text{m}$ depth, where they start to differ significantly. Abrupt transitions during the last glacial, the DO (Dansgaard-Oeschger)

events (Dansgaard et al., 1993), are clearly visible in the Summit cores. Moreover, the high degree of correlation between GRIP and GISP2 leaves no doubt about the possible non-climatic origin of those events.

Along both records 23 DO were identified during the past ~ 15 -100 Kyr. Their evolution appears to develop in three phases: (1) an abrupt warming, whose magnitude ranges from 9 to 16°C degrees (Lang et al., 1999), (2) a gradual cooling and (3) a rapid temperature drop reaching baseline levels.

Overall, the Summit cores provided a wealth of information about the last glacial period providing a clear picture: the stable climate the human race have known in the last few thousands years is nowhere to be seen at least until $\sim 100,000$ years ago (corresponding to ~ 2740 m in fig 2.5). On the contrary, '*change—large, rapid, and global—is more characteristic of the Earth's climate than is stasis*' (Cores, 1997).

The overall success of the Summit programmes and the absence of clear undisturbed Eemian ice at those sites encouraged the establishment of a new consortium in 1995, NGRIP (North GRIP). The location for the new deep drilling project was carefully chosen in order to avoid any possible disturbance in the stratigraphy of the record. Airborne radio echo-sounding (RES) surveys revealed almost perfect conditions, with internal layers' reflections suggesting a correct time-depth relation and a flat bedrock topography (Nixdorf and Goktas, 2001).

The drilling activities lasted for seven years from 1996 to 2003 when the drill hit bedrock or, better, basal water. Already before reaching the bottom, in fact, doubts were raised about the possibility of revealing ice from the penultimate interglacial as the layers' thickness was not decreasing at the estimated rate. Despite a 15% lower precipitation rate than at Summit, at 105 kyr BP (2900m depth) the layers were still about 1.1cm thick, twice as much as by GRIP at the same age (NGRIPmembers et al., 2004). The increased layers' thickness facilitated the dating process because the annual bands were more visible in the record. A new time scale, the GICC05 chronology, was derived based on annual layer counting back to 60.2 Kyr BP (Vinther

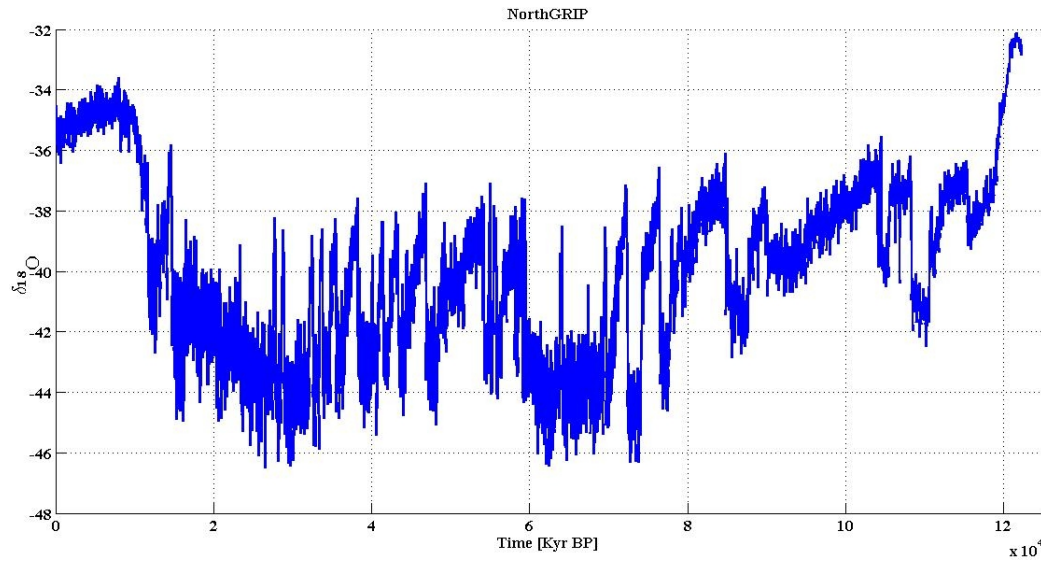


Figure 2.6: NorthGRIP shown on the GICC05modelext time scale (Vinther et al., 2006; Rasmussen et al., 2006; Andersen et al., 2006; Svensson et al., 2008; Wolff et al., 2010).

et al., 2006; Rasmussen et al., 2006; Andersen et al., 2006; Svensson et al., 2008). Beyond this limit, the GICC05 was extended by means of the ss09sea06bm model time scale (shifted to younger ages by 705 years) back until 123 Kyr BP, covering the termination of the Eemian (Wolff et al., 2010).

The reason why the vertical thinning was absent at NGRIP resides in geothermal heat flow, which melts the basal ice. This process has conserved 123 Kyr of ice with very fine resolution; on the other hand, ice older than this age had simply melted away at a 7mm yr^{-1} rate (Dahl-Jensen et al., 2003).

The last (so far) chapter of deep drilling in Greenland is an ongoing story. In 2010, an international organization of scientists from fourteen countries led by the Centre for Ice and Climate at the University of Copenhagen (Denmark) retrieved a new deep ice core as part of the North Greenland Eemian Ice Drilling project (NEEM). This new $\sim 2550\text{m}$ long core was drilled with the specific aim of retrieving the entire, undisturbed sequence of the penultimate interglacial, from its onset to

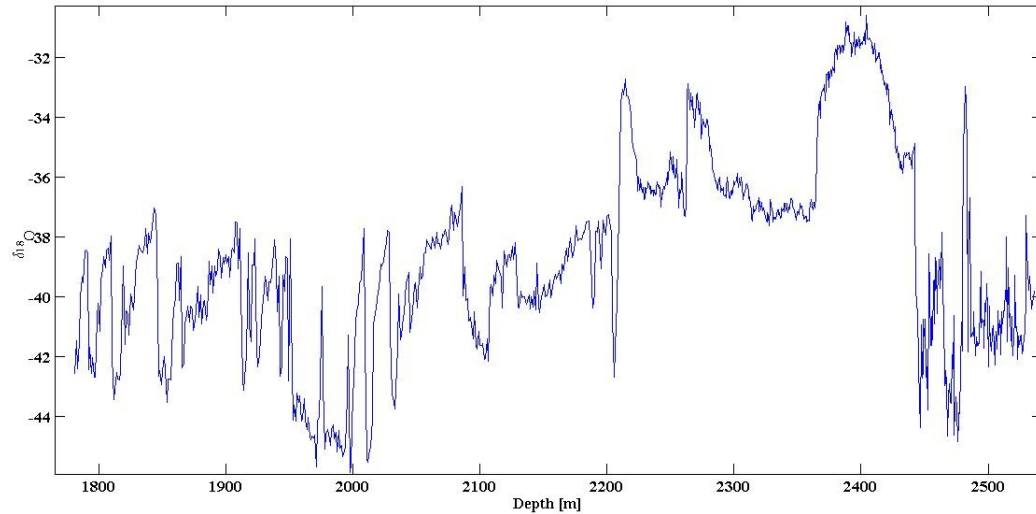


Figure 2.7: Unpublished data (members).

the termination already visible at NGRIP. Once more, though, the stratigraphy of the deepest part of the record appeared to be disordered, as it was at Summit.

In the following, possible reasons for folds in ice sheets and tentative reconstructions of the Eemian sections of ice are discussed.

2.4 Disturbed Eemian ice

Analysis of the NGRIP stable isotopes revealed that in the past interglacial, the Earth have experienced a 5° warmer climate with respect to present day temperatures (NGRIPmembers et al., 2004). Knowledge from the Eemian sequence would give invaluable information about conditions of the Greenland ice sheet exposed to such high temperatures, such as the extent of the ice sheet itself and its possible influence on the climate on a planetary scale. As IPCC previsions estimate a $\sim 2\text{-}6^{\circ}\text{C}$ mean surface air temperature (SAT) increase³ by the end of the 21st century (IPCC,

³This is a unified range of different models applied to several possible scenarios (IPCC, 2007).

2007), investigation of previous comparable periods would strongly help predicting the climate evolution in the near future.

Nevertheless, after six deep drilling projects in Greenland, two of them specifically focused on recovering ice spanning that period, such a complete and undisturbed sequence is still missing. This section summarizes some processes responsible for disturbed stratigraphy of the bottom layers.

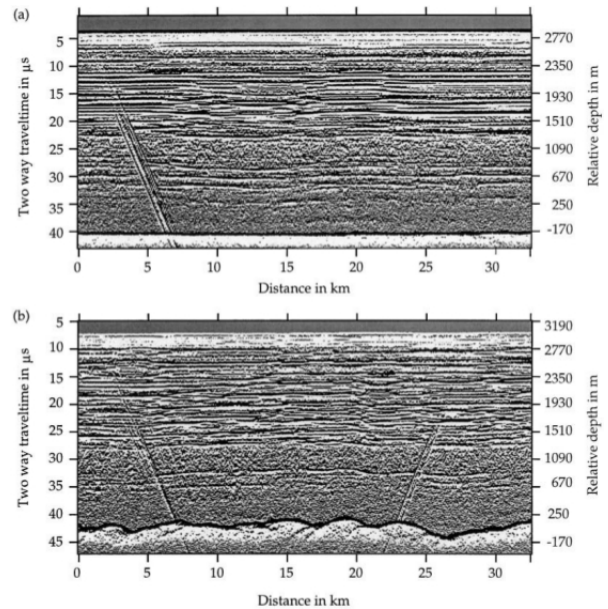
The suggestion that the GRIP core showed climatic instability during the penultimate interglacial period (GRIPmembers et al., 1993) was soon to be abandoned when results from the "twin" core, GISP2, presented a strikingly different pattern prior to ~ 110 Ka BP (Grootes et al., 1993). Analysis of the data, e.g. methane comparisons with Vostok (Antarctica) (Chappellaz et al., 1997), suggested that both cores did contain ice from the Eemian period, if not older. However the stratigraphic order was corrupted by some foldings.

Some mechanisms for explaining these processes have been proposed. For example, the topography of the bedrock. In the case of a non flat bottom surface the flow of the ice can change direction because of undulations or large obstacles along the path. According to Knight et al. (1994), for example, it is likely that the ice above a topographic high will be missing the older layers because of divergence of the flow around the obstacle.

A radio echo sounding (RES) investigation of the areas around NGRIP and GRIP-GISP2 is shown in fig 2.8 (Nixdorf and Goktas, 2001). It is clearly visible that the NGRIP site (upper panel) presents a remarkably flat bedrock, whereas the Summit cores' bottom topography appears more curled. This can be an issue because irregularities at the base might perturb the flow and the layering.

Another possible explanation of the presence of foldings is the ice divide migration. Different cores have proved that the Greenland ice sheet (or at least part of it) has always been present throughout the last glacial cycle, the penultimate in-

Figure 2.8: Radio echo sounding surveys at (a) NGRIP and (b) GRIP. The bed topography is clearly different in the two cases (Nixdorf and Goktas, 2001).



terglacial and earlier. Therefore it has survived to markedly different paleoclimatic conditions and glacial-interglacial transitions. Nevertheless, it is reasonable to think that the position of the ice divide may have moved in time, responding to ice sheet changes. If this is true, its migration would superimpose a shift on the regular flow and contribute in generating the foldings.

A study by Anandakrishnan et al. (1994) concluded that the position of the ice divide in Greenland is mostly sensible to the ice sheet margins' shifts and estimated a lateral migration of 10-50 km. In more recent times, Marshall and Cuffey (2000) studied the evolution of the Central Greenland ice sheet by means of a three-dimensional, thermomechanical model. They predicted ice divide migrations as large as 150 km with abrupt shifts during the last interglacial period in the area around Summit. Fig 2.9 shows an example of a stratigraphic disturbance in the internal layers at the Fletcher Promontory ice cap, Antarctica (Vaughan et al., 1999). The presence of such features under an ice divide were predicted by Raymond (1983)⁴ and observed in the field

⁴These gentle folds under the ice divide are often called Raymond arches, or bumps, in the literature.

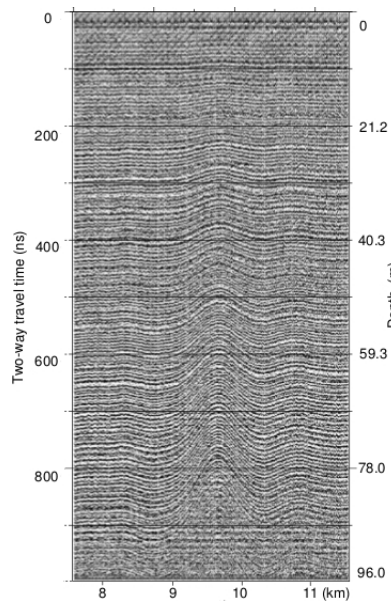


Figure 2.9: Ground penetrating radar (GPR) survey at Fletcher Promontory ice cap (Antarctica) showing a Raymond arch under the ice divide (not visible here). After Vaughan et al. (1999)

for the first time during this survey. When drilling an ice core through this feature, the dating process will deviate from model predictions because the layers are not positioned at the right depths. Nevertheless, being the order of the strata unaltered, the stratigraphy of the record will still be correct. These open folds can still evolve into order disrupting (recumbent) features. According to Jacobson and Waddington (2004), the deformation of an ice sheet in plane strain approximation⁵ can be represented as a combination of pure and simple shear (fig 2.10). In the presence of a Raymond bump the effect of the pure shear is simply to flatten the disturbance (fig 2.10a); the simple shear, instead, will deform and overturn the previously open fold (fig 2.10b). The stratigraphy, in this case, will be corrupted and drilling a core in this position might retrieve ice corresponding to the same age two or three times.

⁵The plane strain approximation is based on the assumption that the flow is developing in two dimensions. Therefore, the third (transverse) dimension can be ignored being the velocity and the strain components null in this direction.

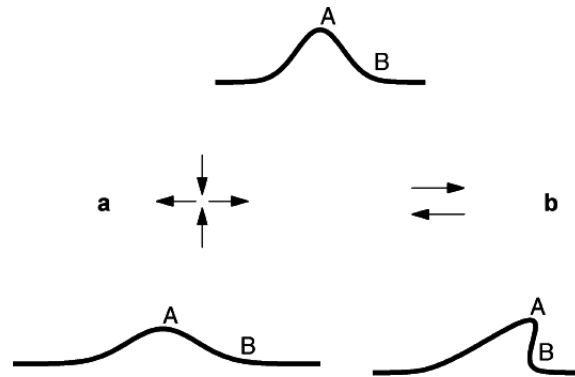


Figure 2.10: The deformation of a disturbed layer under (a) pure shear and (b) simple shear. Pure shear, with vertical compression, flattens the disturbance. Simple shear steepens (and overturns) the A-B limb while leaving the disturbance amplitude unchanged. After Jacobson and Waddington (2004)

2.5 Tentative reconstruction of the last interglacial

So far, ice from MIS-5 in Greenland is clearly visible in three records: GRIP, GISP2 and NEEM. Unfortunately, stratigraphic disturbances have altered the chronology of the cores, therefore preventing to extract climatic information about the Eemian period. Some attempts were done in order to try correcting for the disturbed sections of the Summit cores and extend their dating further than 100 Ka BP. Landais et al. (2003) proposed a method based on comparison of gases globally well mixed in the atmosphere, i.e. whose lifetime is longer than the inter-hemispheric mixing time, between Greenland and Antarctica. Methane CH_4 and oxygen O_2 are good candidates since their residence times in the atmosphere, ~ 10 and ~ 1200 years, well exceed the ~ 1 year inter-hemispheric mixing. The GRIP $\text{CH}_4/\delta^{18}\text{O}$ plane was compared to Vostok (Antarctica), after correcting for inter-hemispheric differences and allowed the authors to propose a tentative reconstruction of the GRIP record. Suwa et al. (2006) subsequently improved this method and applied it to both Summit cores. Their reconstruction is shown in fig 2.11. According to their result, the disturbed sections contain prevalently ice from MIS-5 and MIS-6 (the penultimate glacial) with

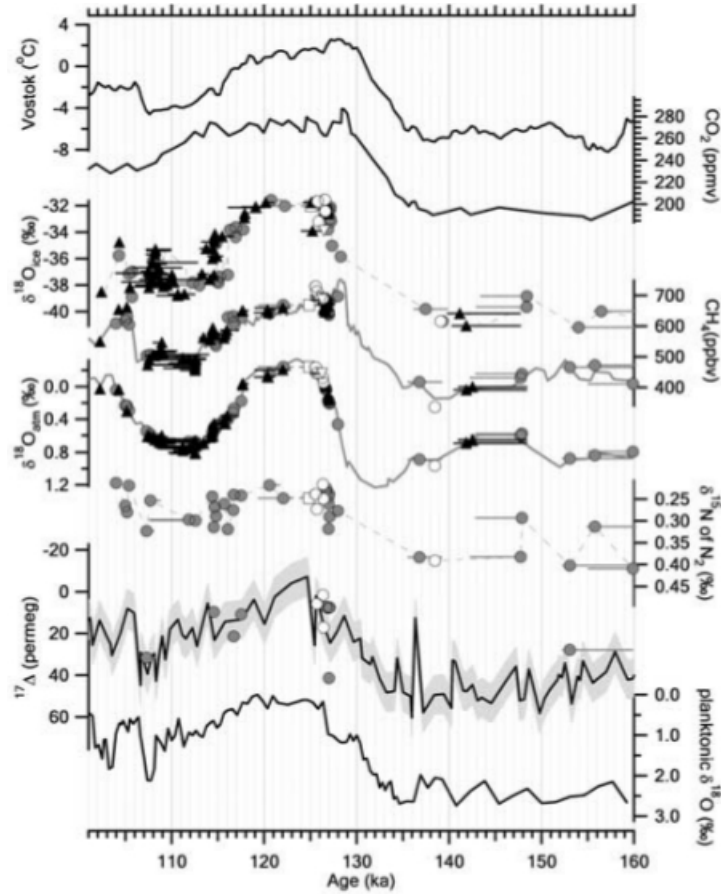


Figure 2.11: Greenland $\delta^{18}\text{O}_{\text{ice}}$ (temperature proxy) compared to Vostok temperature. Also shown are CO_2 , the reconstructed Greenland methane record, the reconstructed $\delta^{18}\text{O}_{\text{atm}}$ record, $\delta^{15}\text{N}$ of N_2 , and $^{17}\Delta$ of O_2 . Shaded circles and solid triangles are the measurements of the disturbed section of the GISP2 core and the GRIP core, respectively, plotted versus best estimate ages. (a) Between 160 ka and 100 ka and (b) between 250 ka and 200 ka. The $\delta^{18}\text{O}_{\text{ice}}$ of planktonic foraminifera from the Iberian margin (MD952042) is also plotted for Figure 9a. After Suwa et al. (2006).

the oldest sample dating back 237 Kyr BP (MIS-7).

At the light shed by the last deep drilling project (NEEM), whose stratigraphy close to the bedrock is once more corrupted, scientific studies dealing with the challenging task of reconstructing a chronologically correct Eemian sequence in Greenland must increase in both number and accuracy. At the end of their paper on ice divide migration, Marshall and Cuffey (2000) shared a thought which seems now quite prophetic. They speculated that '*undisturbed pre-Eemian, and possibly early Eemian, records may never be recovered from the Greenland Ice Sheet*'. Unfortunately, the NEEM record did not prove them wrong. In this perspective, works focusing on this subject acquire even more importance, as they might represent the only way to retrieve information about the oldest ice conserved in the Greenland ice sheet.

Chapter 3

The method

The problem of this thesis is addressed by means of an exhaustive search algorithm. To help understanding the nature of the problem and the way we followed to solve it, we can make use of a comparison with a jigsaw puzzle. A regular puzzle represents a picture of some kind, cut into pieces subsequently given to a player. The difficulty of such a game is mostly dependent on the number of pieces in which the image is split and secondarily on the presence in the image of marked features, easily recognizable. The player will then swap and rotate the given fragments and help his way back to the solution by visually comparing his reconstruction with the original picture. Eventually, with quite some patience, the player will most certainly solve this simple puzzle.

The main idea of this thesis is not conceptually different from the above. In this case, however, there are a number of complicating factors which prevent from being certain to arrive at the true solution of the 'puzzle'. First of all, the starting point is different: following the example above, instead of a picture in pieces, the data used in this thesis represent a corrupted image whose pieces need to be arranged in an unknown way.

The implication of this is of high importance and it represents a major problem in this thesis: the information about size and amount of the fragments is not preserved.

We are left with guessing where the original picture was cut before doing anything else. On top of that, the operations allowed on each piece are not well defined as it was the case in the example above where swap and rotation would eventually bring the player to the solution. Instead, we have to decide which operations to apply. Therefore, even assuming to know how to split the picture, it would not be sure to accurately recreate the original structure. Furthermore, the amount of configurations created applying the decided operations on each piece precludes us the possibility to readily verify by eye whether one of them is consistently better than the other ones. An automated routine has to be created, which is able to determine the best configuration. This gives rise to yet another important issue of this work. What is the best configuration? With a jigsaw puzzle, the player knows his goal, the original image. This is not the case here. So far, no ice core drilled in Greenland has presented a continuous and uncorrupted section of ice spanning the whole Eemian interglacial. It is thus necessary to look for this period in Antarctic cores. In this case, however, a comparison is not straightforward (see chapter 4).

On this basis, an algorithm was developed in order to perform the steps just outlined. The *Main* program consists of the three following blocks:

- *Splitting* : the folded section of data is divided into n intervals
- *Operations*: generation of candidate solutions
- *Match*: each configuration is matched to a 'reference' function (see chapter 4)

All the steps are described in detail in the following sections. It should be underlined that this work is not connected to any ice flow model and it is not supposed to give a precise answer regarding detailed length and amplitude of the penultimate interglacial. Nevertheless, it is a very useful exercise which may suggest a robust rearrangement of the data resulting in a qualitatively correct Eemian section.

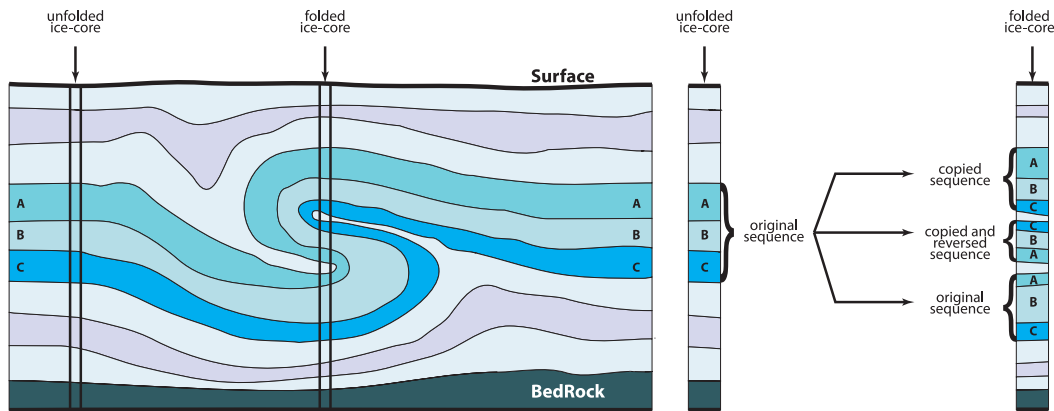


Figure 3.1: Sketch of a recumbent folding. An ice core drilled through this feature would retrieve the layers A-B-C at least twice; the second section is inverted in depth.

3.1 Generation of candidate solutions

As it was described in section 2.4, deformations under an ice divide can be represented by pure and simple shear (Jacobson and Waddington, 2004). The simple shear operates parallel to the isochrones and in the presence of a disturbance, bend it producing a deformation which can alter the chronology of the ice. A sketch of such a situation, called recumbent folding, is given in fig 3.1. If an ice core was drilled through such a feature, the same layers (A-B-C in the figure) would be collected twice or even three times, where the second section would be in principle identical to the first one, but reversed in depth (C-B-A).

This fact led to the choice of operations to apply to the data. Their combined use generate a given amount of candidate solutions which are subsequently tested by *Match* (see 3.2).

The corrupting processes responsible for the ice foldings are idealized into three discrete operations:

1. *Copy*: one or more intervals are considered to be the duplicate of another interval and are therefore cancelled;

2. *Reverse*: one or more intervals are reversed respect to the x-axis (depth or time);
3. *Interchange*: the order between the intervals is altered choosing one of all the possible permutations between them.

The above list represents the *Operations* block.

Copy and *Reverse* both generate $\Pi_c = \Pi_r = 2^n$ options, where n is the amount of intervals into which the original data series is split and 2 is the number of possible states for each operator. Erased or conserved in the former case, reversed or straight in the latter. *Interchange*, instead, produces $\Pi_i = n!$ different profiles, all the possible permutations of the n intervals.

This is illustrated in Table 3.1 by the matrices used to construct the candidate solutions. The columns (Roman enumeration) identify the n intervals; the rows are the generated configurations.

In Table 3.1a, '0' stands for the removal of the corresponding interval. Therefore, *Copy* actually produces only $\Pi_c = 2^n - 1$ profiles, as the null configuration (all 0 in the corresponding matrix, highlighted in red in table 3.1a) is discarded.

Table 3.1b, instead, shows all the possible combinations of *Reverse*. The direction of the arrows indicates whether an interval is inverted or not (straight is from left to right). Finally, table 3.1c lists all the possible permutations of the intervals.

The three operators are applied together to produce $\Pi = \Pi_c \cdot \Pi_r \cdot \Pi_i$ configurations. However, the order of application is important: *Copy* must be in the first place. In fact, the configurations generated by this operator always have $m < n$ intervals, beside for the last option in which $m = n$ (row 7 in 3.1a). As a consequence, identical configurations will be generated if *Reverse* or *Interchange* are applied before the third operator.

An example will clarify this issue. Say *Interchange* is applied first to a function divided into $n = 3$ intervals. The output is given in table 3.1c. Removal of a given interval, e.g. III, will result in three couples of identical solutions. This is shown

	I	II	III
0	0	0	0
1	1	0	0
2	0	1	0
3	0	0	1
4	1	1	0
5	1	0	1
6	0	1	1
7	1	1	1

(a) *Copy*: '0' stands for removal.

	I	II	III
1	↔	↔	↔
2	→	↔	↔
3	↔	→	↔
4	↔	↔	→
5	→	→	↔
6	→	↔	→
7	↔	→	→
8	→	→	→

(b) *Reverse*: ↔ stands for inversion.

	I	II	III
1	III	II	I
2	III	I	II
3	II	III	I
4	II	I	III
5	I	II	III
6	I	III	II

(c) *Interchange*: permutations of the intervals

Table 3.1: Configurations generated by the *Copy* (a), *Reverse* (b) and *Interchange* (c) operators when applied separately to a function divided into three intervals ($n=3$). Intervals have Roman enumeration (columns). Rows are configurations. Respectively, $\Pi_c=2^3-1=7$; $\Pi_r=2^3=8$; $\Pi_i=3!=6$.

in table 3.2. Since *Copy* routinely removes one or more intervals, this process will happen different times producing an erroneous amount of configurations, where many will be identical. With $n=3$, Π would be:

$$\Pi_{wrong} = (2^n - 1) \cdot (2^n) \cdot n! = 7 \cdot 8 \cdot 6 = 336 \quad (3.1)$$

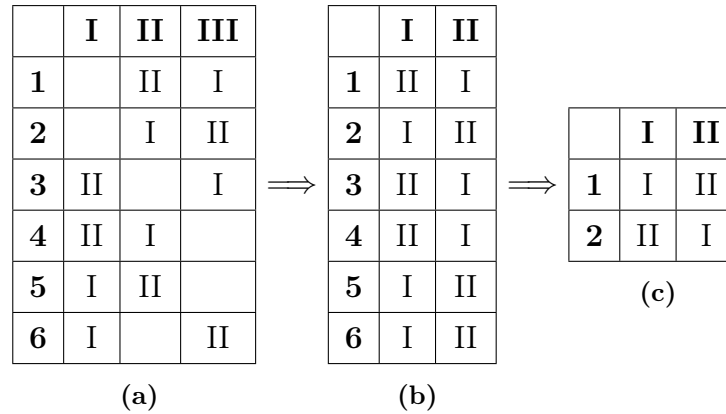


Table 3.2: Example of generation of identical configurations. (a) *Interchange* is applied to a function divided into $n=3$ intervals. (b) Interval III is erased (part of *Copy*), producing three couples of identical combinations (b-c).

To avoid this problem, the operators are used in sequence. First, *Copy*, which produces Π_c configurations. Subsequently, *Reverse* is applied to each option previously generated. This step splits each Π_c into $\Pi_r=2^k$ different options, where k is the number of intervals not deleted. At last, *Interchange* generates $\Pi_i=k!$ for each Π_r . A graphical scheme of the cascade of configurations produced by *Operations* when $n=3$ is given in fig. 3.3.

The total amount of profiles generated by the three operators, avoiding repetitions, is given by:

$$\Pi = \sum_{k=1}^n \binom{n}{k} \cdot 2^k \cdot k! \quad (3.2)$$

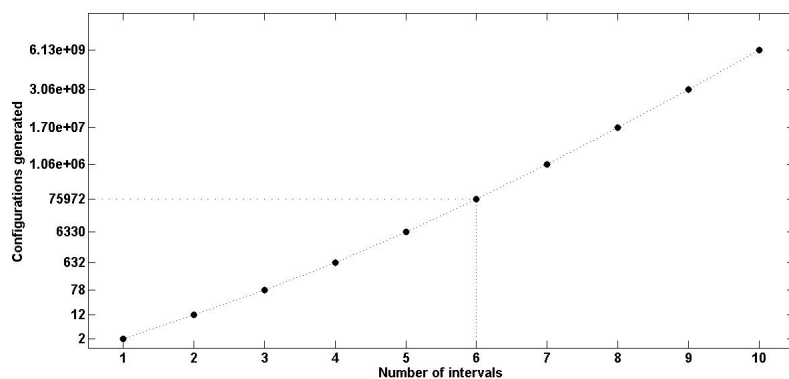


Figure 3.2: Amount of configurations generated by *Operations* on a semi-log scale. Π roughly grows by one order of magnitude per unit increase in n . Already at $n=6$, $\Pi=75972$.

where n is the number of intervals. The binomial coefficients $\binom{n}{k}$ give the number of configurations composed by k intervals:

$$\binom{n}{k} = \frac{n!}{k!(n-k)!}, \quad k \in [1, n] \quad (3.3)$$

In fig. 3.2, the generated profiles Π are plotted against the number of intervals n . The y-axis is logarithmic. It is straightforward to see that the rise in Π is steep, roughly one order of magnitude per unit increase in n . This fact poses a computational limit when all the options have to be matched to a reference profile.

3.2 The match function

As seen in fig. 3.2, dividing the original data series in three parts will produce 78 possible reconstructions of the Eemian. This simple fact makes it challenging to check the generated profiles manually and to select the profile whose most accurately reproducing the penultimate interglacial. Many configurations will be probably meaningless. Nonetheless, all of them must be checked in order to decide which one is the best. In order to attain this, an algorithm is developed, which performs a comparison between two given functions y_1 and y_2 and calculates the best translation and scale

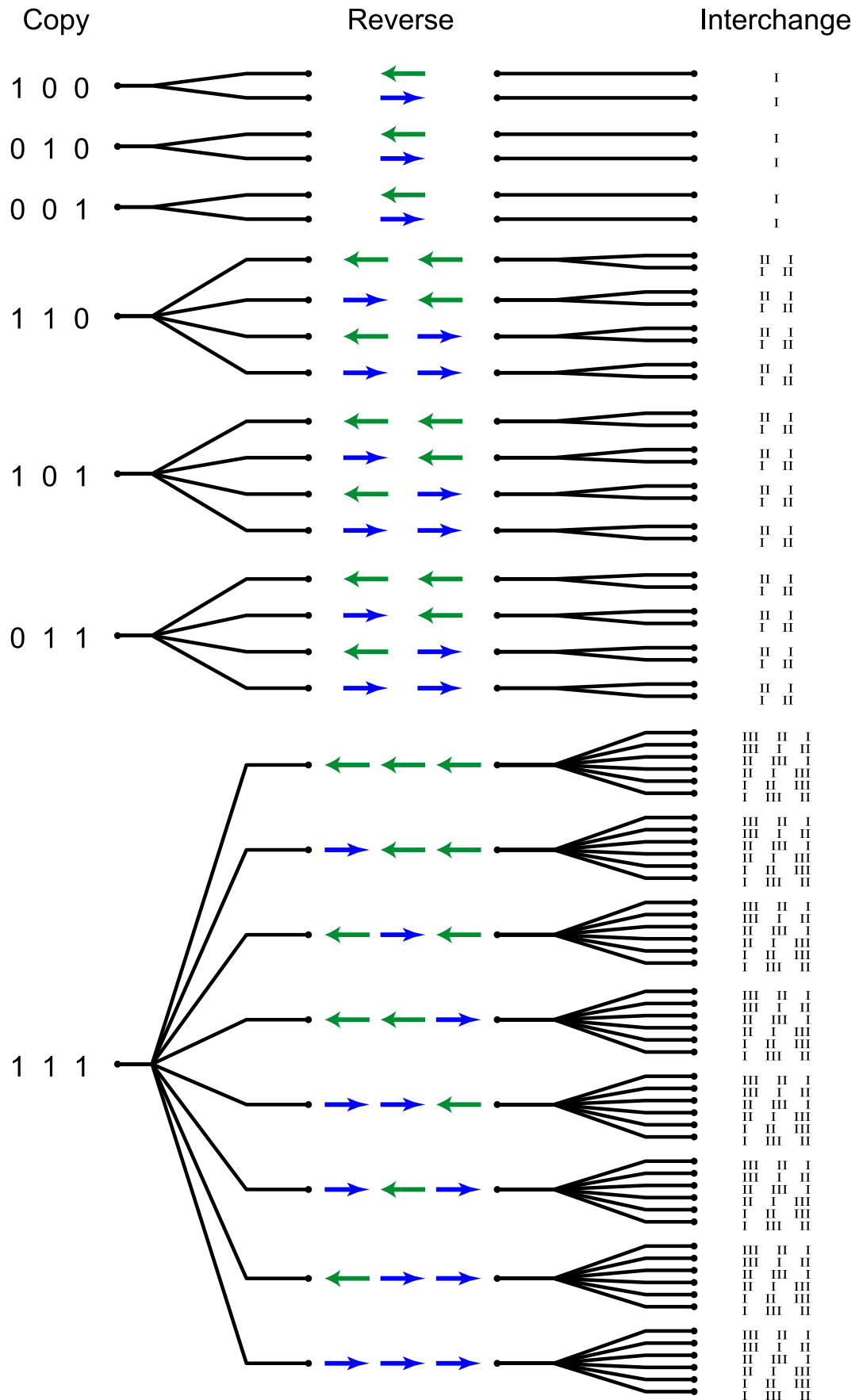


Figure 3.3: Cascade of configurations generated by *Operations* when $n=3$.

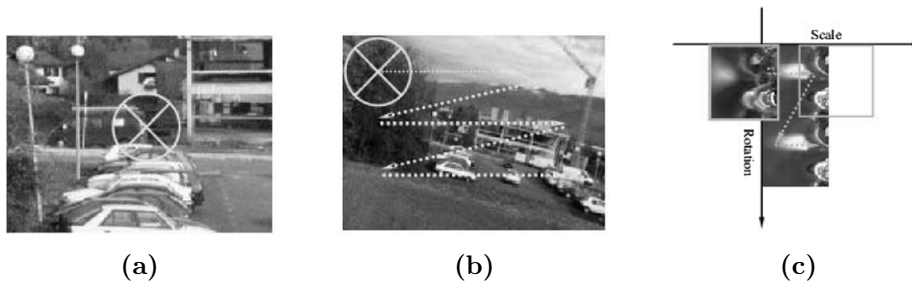


Figure 3.4: Four-dimensional search strategy. (a) A circular template from the center of the reference image is cropped. (b) For every position in the target image, a circular region is selected and compared against the circular template in (a) to find the best (T_x, T_y) . (c) Search for (R, S) in the log-polar domain. After Zokai and Wolberg (2005), fig 7.

factors needed to align them. It is worth noting the generality of such a program, as it is in no way connected to stable isotopes profiles or more in general to ice core data. The two input functions can, in principle, be anything.

In the following section (see Algorithm), it is described how this program, *Match*, works. Prior to doing so, a work which is at the basis of the routine developed in this thesis is introduced.

The routine described below finds its origins in a paper about image registration (Zokai and Wolberg, 2005). In their work, the authors introduced a hybrid algorithm able to automatically align image pairs in the presence of significant similarity transformations (scale, translation, rotation) and moderate perspective changes. They used different methods to address these two problems. The first task is accomplished by means of the log-polar transform (LPT) and finds the best scale, translation and rotation values, aligning the two images. Subsequently, the Levenberg-Marquardt non-linear least squares optimization (or simply L-M algorithm, LMA) is used in order to correct for perspective deformations. The LMA permits to achieve sub-pixel precision.

As perspective is not an issue in our problem, we can focus on the first part of

their algorithm, the LPT method. The transformation is given by:

$$r = \log_b \left(\sqrt{(x - x_c)^2 + (y - y_c)^2} \right) \quad (3.4a)$$

$$\theta = \tan^{-1} \left(\frac{y - y_c}{x - x_c} \right) \quad (3.4b)$$

where the base b can be chosen by the user¹.

The effectiveness of this approach can be explained by two short examples. Consider two images I_1 and I_2 and their polar transforms I_{1p} and I_{2p} , where the second picture is a rotated version of the first.

- 1) Crop central region I'_1 from I_1 .
- 2) Compute I'_{1p}
- 3) For all position (x, y) in I_2 :
- 4) Crop region I'_2 .
- 5) Compute I'_{2p} .
- 6) Cross correlate I'_{1p} and $I'_{2p} \rightarrow (dx, dy)$.
- 7) If max corr, save (x, y) and (dx, dy) .
- 8) Scale $\leftarrow dx$.
- 9) Rotation $\leftarrow dy$.
- 10) Translation $\leftarrow (x, y)$.

Table 3.3: LPT algorithm from Zokai and Wolberg (2005). The procedure is applied recursively from coarse to fine resolution.

Then, I_{2p} will be equal to I_{1p} , shifted along the θ -axis. The shift $d\theta$ will then correspond to the maximum of the cross correlation between the two. The same reasoning works with the radial coordinate, but the use of logarithm is essential.

For the product property of the log function:

$$\log(\alpha x) = \log(\alpha) + \log(x) \quad (3.5)$$

where α is a constant. For this reason $(\alpha x, \alpha y)$ is mapped to $(\log \alpha x, \log \alpha y)$ in the log-space, which can be rewritten as $(\log \alpha + \log x, \log \alpha + \log y)$. It is evident now that a scale factor α in the Cartesian space is equivalent to a phase

shift in the logarithmic space. Maximizing the cross correlation in the latter domain will give the best $d(\log r)$ and $d\theta$, which represent scale and rotation in Cartesian space.

As depicted in table 3.3, the authors proceeded by cropping a circular region¹ of the first image I_1 and computing its LPT, I'_{1p} (where ' denotes the crop). Then they cross correlate in the log-polar space I'_{1p} with the LPT of cropped regions of the second image I'_{2p} for different positions (x, y) (see fig. 3.4). The best match is

¹In Zokai and Wolberg (2005) the radius is 25% of the image width and the center of the cropped region is positioned at the center of the image. The base is calculated as $b = \exp(\log(w)/w)$, where w is the width of the image, in order for the transformed image to have the same width of the original.

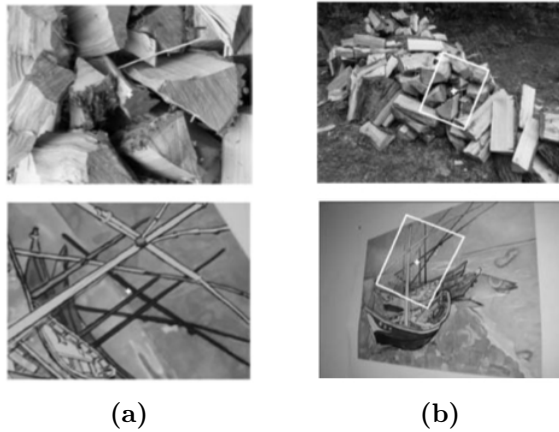


Figure 3.5: (a) Observed images: 4 zoom, arbitrary rotation, and moderate perspective. (b) Registration results highlighted on reference images. After Zokai and Wolberg (2005), fig 8 (selection).

selected through the normalized correlation coefficient similarity measure:

$$\langle I_1 \circ I_2 \rangle = \frac{\sum(I_1 - \mu_1)(I_2 - \mu_2)}{\sqrt{\sum(I_1 - \mu_1)^2(I_2 - \mu_2)^2}} \quad (3.6)$$

where μ is the average of the corresponding image. The algorithm is applied recursively from coarse to fine resolution. At each step the resolution is increased and a neighbourhood of the best match values limits the search space of the new cycle.

This hierarchical system permits to save computing time as most of the operations are done at the coarsest level. Some examples of the performance of such a combined method are given in fig. 3.5, which shows the successful registration of two image pairs selected from their work.

The algorithm

The results in fig. 3.5 show the goodness of the procedure used by the authors. Nevertheless, comparing images and ice core data profiles are two quite different tasks and the methods applied to perform such matches must change accordingly. First of all, they dealt with pictures, 2D data, while 1D functions are in focus here. The immediate implication of this is that it is unnecessary to include rotation as one of the possible similarity transformations. It is thus possible to drop eq. 3.4b and simplify the log-polar transform to a 'log transform'.

Moreover, the normalised cross correlation similarity measure in 3.6 does not necessarily represent the best choice when applied to ice core data profiles. It makes perfect sense, e.g., to remove the mean when comparing images; in that case, in fact, different luminosities might interfere with the matching process. However, as described in the previous chapter, the Dansgaard-Oescher events during the last glacial share very similar but still different amplitudes. Manipulations on the data, such as removing the mean or performing some kind of normalization, might alter such modest but distinguishing marks. Therefore, it was decided not to apply any such operation, unless strictly necessary. Moreover, a formula based on squared differences was introduced, which represents the distance between the two functions.

At last, the two input functions are not cropped in any way inside *Match*, like in Zokai and Wolberg (2005). It is possible to select a piece of y_1 to be compared to a piece of y_2 , if desired by the user, but it is not part of the matching algorithm. This is again due to high self-similarity of ice core data. Whenever possible, it is preferable to use longer stretches of data in order for the program not to fall in wrong but not meaningless matches.

0. The concept

Conceptually, the algorithm works with two cycles: one over the possible translation factors and a second one over the selected scale factors. At each step in these cycles a (i, j) couple corresponds to a different (dx_i, s_j) pair. As in the cited work above, the scale search takes place in the logarithmic space, after the log-transform is applied. The function y_2 is translated by dx_i in the Cartesian space and by $\log(s_j) = dr_j$ in the log-space, before the goodness of the match between \bar{y}_{2p} and \bar{y}_{1p} is estimated through squared differences.

If specified by the user, at the end of the cycles the two input profiles are exchanged and the program runs once more. The reason for this is specified in the text below.

1. The grid

First step is to define a rectangular grid $\mathcal{N} \times \mathcal{S}$, where $\mathcal{N} : \{dx_i, i = 1, \dots, N\}$

and $\mathcal{S} : \{s_j, j = 1, \dots, S\}$ are the parameters' domains and N, S specify their dimensions. The translation array \mathcal{N} is defined by the x-axes of the two input functions. Imagine \bar{x}_1 and \bar{x}_2 to be defined in the $[a, b]$ and $[c, d]$ ranges, respectively. The second profile is first horizontally shifted to zero and then translated by a quantity dx :

$$\bar{x}_2 = \bar{x}_2 - x_2(c) + dx_i \quad . \quad (3.7)$$

The first and last elements of the translation vector are dependent on \bar{x}_1 initial and final values, defined in the following way:

$$\bar{x}_2 = \bar{x}_2 - x_2(c) + \overbrace{x_1(a)}^{dx_1} \quad (3.8a)$$

$$\bar{x}_2 = \bar{x}_2 - x_2(c) + \underbrace{x_1(b) - \alpha \cdot \overbrace{(x_2(d) - x_2(c))}^{x_2 \text{ length}}}_{dx_N} \quad . \quad (3.8b)$$

Therefore, the first element of \mathcal{N} corresponds to the first component of \bar{x}_1 . Instead, dx_N is defined as the last coordinate of \bar{x}_1 , modulated by α times the length of x_2 , where $\alpha \in [0, 1]$ denotes the minimum fraction of \bar{y}_2 which the user wants to superpose over \bar{y}_1 . Once the number of elements N has been set, the other components of \mathcal{N} will uniformly fill the space between dx_1 and dx_N in $N-2$ steps.

On the other hand, the \mathcal{S} space is left at will of the user and have to be specified depending on the problem at hand. If any clue about a possible range of scale values is known, \mathcal{S} should be set accordingly. Otherwise, a more general range including values both smaller and bigger than one must be defined. In the following of the thesis, \mathcal{S} is imposed to span the $[0.2, 2]$ range, if not otherwise specified.

In order to equally represent both spaces below and above unity, the intermediate values span \mathcal{S} only semi-uniformly. This modification must be included in order to fairly represent the $\mathcal{S}_{left}=[0.2, 1]$ and $\mathcal{S}_{right}=(1, 2]$ spaces.

Increasing or decreasing both N and S affects the resolution of the grid and by consequence the precision of the program. For the scale factor search, $S=50$ is sufficient to have a satisfactory resolution as this imposes an average step ds approximately equal to 0.036 between each s_j and s_{j+1} with \mathcal{S} defined above. The choice of N is more delicate as \mathcal{N} is not fixed, but dependent on the length of the two input functions.

2. The cycles and the log-transform

Once the grid is specified, two loops, one embedded in the other, span the corresponding arrays. The logical steps are outlined in table 3.4. The outer loop is performed over the \mathcal{N} array. After applying the translation dx_i to \bar{x}_2 (1), both \bar{x} vectors are shifted to the new origin dx_i and the logarithm is taken (2). The last operation produces the two \bar{r} vectors. The points of \bar{r}_1 lying at the left of the new origin will produce a complex logarithmic coordinate and will be discarded. Moreover, the first element of \bar{r}_2 will be infinite by definition and must be removed as well (3a-3b). The first three steps are visible in fig 3.6 for two example functions.

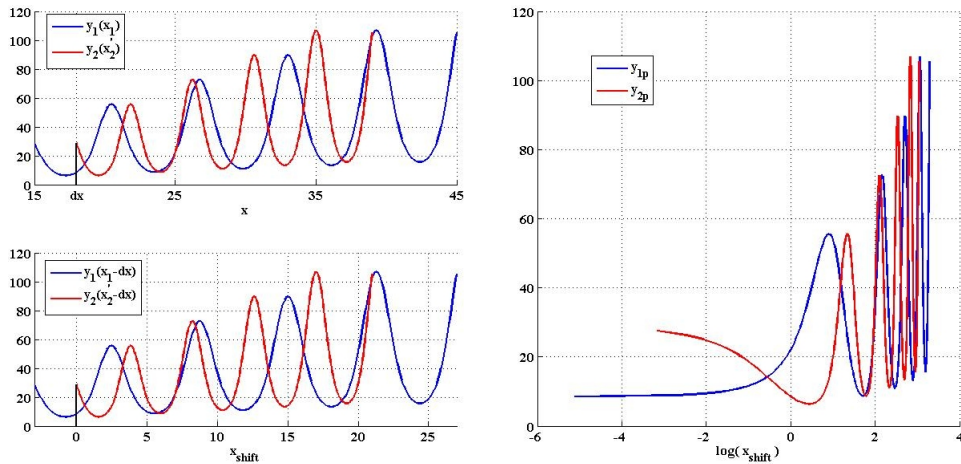
For each increment in the variable i , the inner cycle is performed over \mathcal{S} . The corresponding scale factor s_j is applied to \bar{r}_2 in form of a translation in the log-space (4). This corresponds to horizontally shifting the red function in 3.6b. Finally, when both the affine transformations are applied, the squared point-to-point difference between the transformed functions is taken (5). The details of the last step are given in the next paragraph.

3. The match

The match between y_{1p} and y_{2p} is calculated by squared differences. So far the two functions may have had different x-axes, even non-uniformly spaced, but before evaluating the point-to-point distance between them it is necessary that the transformed profiles share a common grid. Therefore, the overlapping region of y_{1p} and y_{2p} is selected and a uniform vector $\bar{r}_{new} : \{r_{new}(k), k = 1, \dots, M\}$ is defined in the log-space. A linear interpolation is then performed on the two

cycle 1 (dx_i)	
1)	$\bar{x}'_2 = \bar{x}_2 - x_2(c) + dx_i$
2)	$\left. \begin{aligned} \bar{r}_1 &= \log(\bar{x}_1 - dx_i) \\ \bar{r}_2 &= \log(\bar{x}'_2 - dx_i) \end{aligned} \right\} \text{log transform}$
3a)	$\bar{r}_1 = \bar{r}_1 \mid r_1(m) \neq \pm Inf \quad \wedge \quad r_1(m) \in \mathcal{R}, \forall m$
3b)	$\bar{r}_2 = \bar{r}_2 \mid r_2(m) \neq \pm Inf, \forall m$
cycle 2 (dr_j)	
4)	$\bar{r}'_2 = \bar{r}_2 + dr_j$
5)	(y_{1p}, y_{2p}) match
end	
end	

Table 3.4: Logical steps of the cycles



(a) Cartesian space. (Top) Step (1) of table 3.4. (Bottom) Shift to the new origin.

(b) Logarithmic space. Real part of the log transformation of (a) bottom panel.

Figure 3.6: Steps (1-3) of table 3.4 for two synthetic functions y_1 and y_2 , where the latter is a rescaled and translated version of the former. The second step is split in (a) bottom and (b).

profiles over this new axis. The extremes of \bar{r}_{new} are selected as the biggest minimum and smallest maximum of the previous \bar{r}_1 and \bar{r}_2 vectors. In this way, the interpolation always takes place in regions where the information about both functions is available, i.e. extrapolation of data points is not allowed. Once both selected profiles are interpolated on the common vector, their distance D is calculated by squared differences in the following way:

$$D(i, j) = \sqrt{\sum_{q=1}^M (\tilde{y}_{1p}(q) - \tilde{y}_{2p}(q))^2} \quad (3.9)$$

where the $\tilde{\cdot}$ denotes the interpolated functions in the logarithmic space. The closer this number is to zero, the better the two functions overlap.

Each (i, j) pair in the grid will then correspond to a $D(i, j)$ distance point. The ensemble of all these points will form a surface, whose most pronounced minimum D^* represents the translation and scale factors (dx^*, s^*) which best align y_2 to y_1 . The grid will then be refined around the best guess $D^* \rightarrow (dx^*, s^*)$ before running the routing one more time (see next step).

The normalized correlation coefficient used by Zokai and Wolberg (2005) was tested as well, but as anticipated above in the text it is not suitable in this context. In the same way, the covariance between the functions, defined as:

$$cov(\bar{y}_1, \bar{y}_2) = \sum_{k=1}^K \frac{(y_1(k) - \langle y_1 \rangle) \cdot (y_2(k) - \langle y_2 \rangle)}{K} \quad (3.10)$$

did not produce a better result than D in 3.9.

Grid choice

The distance equation 3.9 is evaluated on a uniformly spaced grid in the logarithmic space. It is important to understand whether there is any difference in the output surface D when the squared point-to-point difference is calculated on a grid that is uniform in such a domain or in the Cartesian space.

In this box, two examples are investigated in order to address this question. In fig 3.7, one synthetic profile is drawn in different colors, representing different samplings. Furthermore, each function is coupled to one of its possible rescalings, constructing the two pairs f_1-f_2 in blue and g_1-g_2 in red. Accordingly, their squared point-to-point differences shall be denoted D_f and D_g , respectively. These functions correspond to a slice of the distance surface mentioned above for a given dx_i ; in particular, for the right dx as it will be clear further on. The panel on the right shows the log-transforms $f_{1p}-f_{2p}$ and $g_{1p}-g_{2p}$ with respect to x_0 , the pivot of the transformation (black dot in 3.7a). The coloured dots represent the sampling of the data sets: uniformly spaced over x in blue (3.7a) and over $\log(x)$ in red (3.7b).

In the former case, the corresponding points in the log-space are more sparse close to the pivot; for this reason the ending part of f_1 and f_2 , where they differ more, will have a bigger weight when calculating their difference D_f . On the other hand, when the sampling is uniform in $\log(x)$, the same profiles' distance will be driven mainly by the area close to x_0 , therefore resulting in a smaller value. As a consequence of this, D_g , the distance surface evaluated in the uniform log-space, will be closer to zero than D_f . This is not very interesting and useful per se, as an approximately constant shift would not lead to the selection of a different minimum in the surface (see the thin blue and red lines in fig 3.8). Nevertheless, it is possible to see that such a minimum is sharper in the Cartesian space and therefore less likely to be captured there, unless the scale domain \mathcal{S} is very refined. Fig 3.8 shows the scale factor search for the two f and g pairs, characterised by different grids. The shaded thick lines are running means of the two $D_{f,g}$ functions. As expected, the blue curve, corresponding to the grid uniform in x , settles on a higher mean value with respect to the red line (grid uniform in $\log(x)$). Moreover, it is visible that the trough in the red profile is broader. Furthermore, D_g gently curves towards the minimum, as pictured by the shaded red line, while the blue curve D_f is

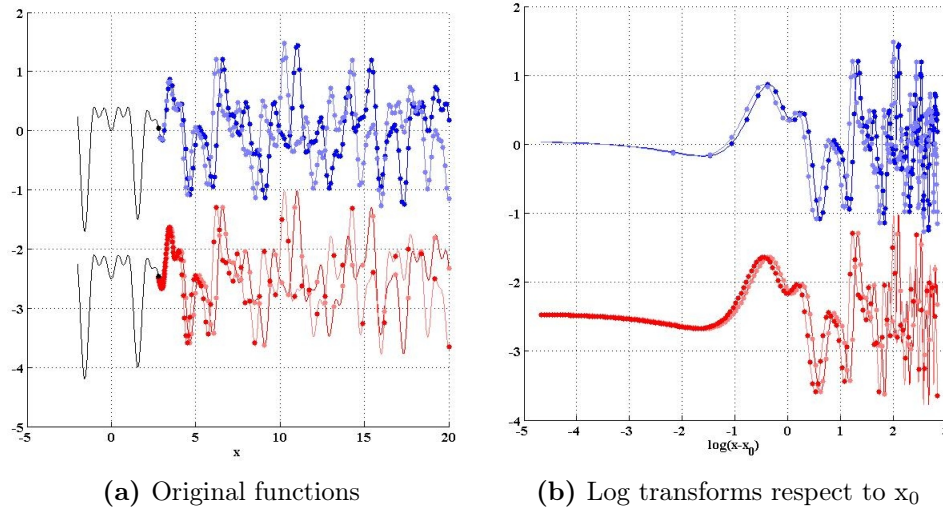


Figure 3.7: Pairs of synthetic profiles f_1 - f_2 (blue) and g_1 - g_2 (red) with uniform sampling in the Cartesian (a) and logarithmic (b) space, respectively. The pivot of the transformation is x_0 (black dot, left panel). Functions f_2 and g_2 are rescaled versions of f_1 and g_1 .

quite flat on the whole domain beside a very narrow region around the correct scale factor. Consequently, when defining the \mathcal{S} domain (coloured dots in the figure), it will be more challenging to spot the right scaling if the search space is uniformly sampled over x instead of $\log(x)$. In the example shown in fig 3.8, the minima selected in the two grids are highlighted; D_f^* , the minimum of D_f respect to the shown blue sampling, falls well out of the right trough. Moreover, the neighbourhood of D_f^* has a pronounced local minimum, which would be selected for any sampling not fine enough to have at least one data point in the very narrow region around the correct scale factor. In comparison, the range where one data point would be safely selected as D_g^* in the red sampling is much broader than $I(D_f^*)$.

In conclusion, this example shows that it is safer to calculate the squared distance D in equation 3.9 on a uniform grid in the logarithmic space. For an

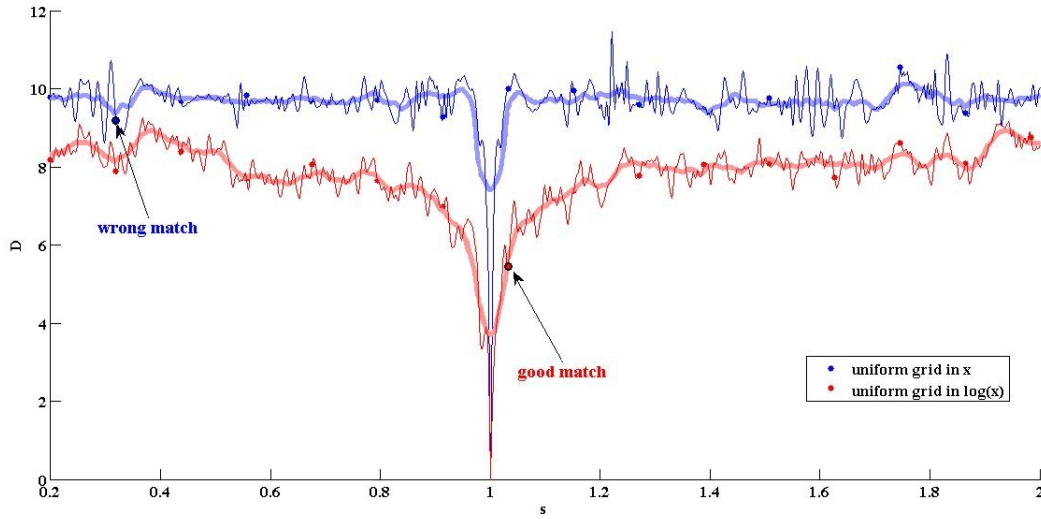


Figure 3.8: Scale factor search with uniform grid in the Cartesian (blue) and logarithmic (red) space. Dots represent discrete samplings in the two spaces. The best choice for each case is highlighted. The shaded lines are running means of the infinitely refined samplings (thin lines). The trough is broader in the log space and therefore more easily detected.

infinitely refined \mathcal{S} domain there is no difference (thin lines in fig 3.8), but for a discrete sampling the result is more robust in the log-space.

4. Neighbourhood and grid refinement

Once the minimum $D^* \rightarrow (dx^*, s^*)$ is selected, the grid is refined in both search spaces \mathcal{N} and \mathcal{S} in a neighbourhood of the selected best guess. Two parameters tune both the size of such area (1) and the number of elements added to the previous arrays (2). As the resolution needed in the two of them might differ, these parameters are set independently for \mathcal{N} and \mathcal{S} .

The neighbourhoods are defined as:

$$I_{dx^*} = \{dx^* - \kappa, dx^* + \kappa\} \quad (3.11)$$

$$I_{s^*} = \{s^* - \sigma, s^* + \sigma\} \quad . \quad (3.12)$$

Subsequently, between each value of I_{dx^*} and I_{s^*} , p and q elements will be added, respectively.

A graphical example of a fictitious match is shown in fig 3.9 with an initial $N \times S = 6 \times 7$ grid. At the first cycle, the resolution is coarse in both search spaces. Once the best pair is selected (red dot), a neighbourhood of the point is taken and new (dx, s) pairs refine the grid (green dots at cycle two). This process is then repeated a third time. Note that each grid still conserves some data points from the previous cycles (black dots at cycle two; black and green dots at cycle three). In these points there is no need to perform new computations.

Therefore, the resolution can be increased at will in the two domains, independently. Such routine performs the calculations in a computing-wise manner. In fact, the calculation efforts are increasingly focused in the area of interest.

It is given implicit in this approach, that the specific neighbourhood where the "true" minimum of the distance surface lies can be found at the first cycle. If this is not the case, the algorithm will inevitably focus on a local minimum, thus producing a wrong result. This issue is described in better details in the next section.

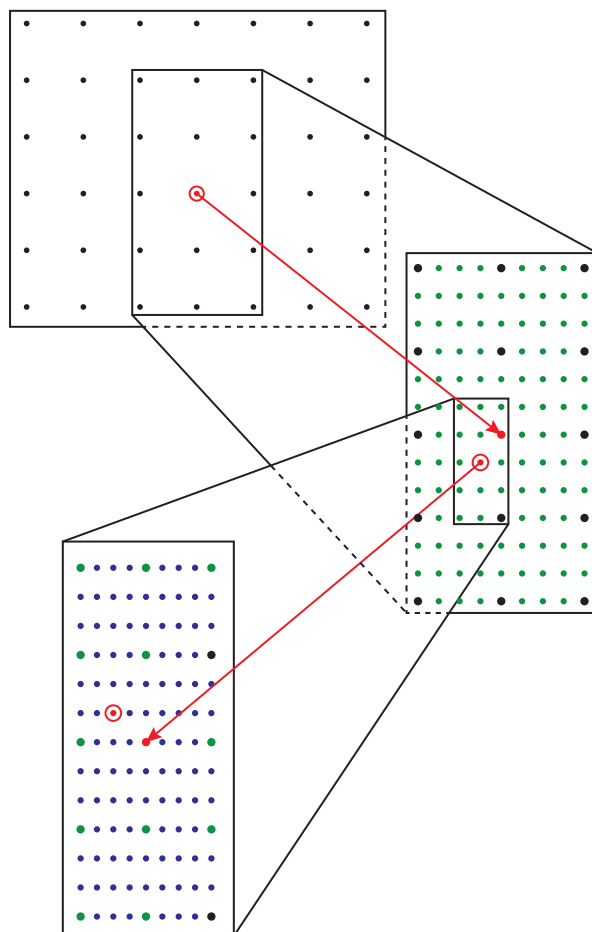


Figure 3.9: Three cycles of refinement are shown. The initial grid (black) has $N \times S = 6 \times 7$ elements. The neighbourhoods' sizes are set to $\kappa = 2$ and $\sigma = 1$, around (dx^*, s^*) (red dot). The new grid (green) is formed by this area, filled with $p = 2$ and $q = 3$ new elements along the \mathcal{N} and \mathcal{S} dimensions, respectively. The whole process runs once more producing the blue grid. Note that the points of the previous grid, which are inside the neighbourhoods, are conserved throughout the cycles (black dots in the green grid; black and green dots in the blue grid).

3.3 Test

The grid refinement process

Since the *Match* algorithm is the core of the *Main* program, different tests were performed in order to check its reliability.

The first test addresses the issue introduced at the end of the previous section. As shown in chapter 2, some of the abrupt DO events occurring during the last glacial cycle have similar magnitude and duration. For this reason, using a coarse resolution in the \mathcal{N} domain can produce a mismatch. This issue can be better understood by the use of an image. In fig 3.10 a mismatch situation is given. The upper panel shows NGRIP $\delta^{18}\text{O}$ profile versus depth; highlighted in red are the DO number 19, 20 and 21. This section is then matched to the blue curve using a poorly ($N=50$) refined translation grid. The mismatch is visible in the lower panel: the result matches the above events to DO 11 to 15. Considering the particularly small amplitude of DO-13 and short duration of DO-15, the visible result is not unreasonable. Such a situation arises because the \mathcal{N} vector does not include an element close enough to the right dx^* factor. However, the selected section (red in the figure) has a very similar structure to other parts of the record and another consistent but wrong result is estimated. At the second cycle, if the neighbourhood is not large enough to include dx^* , the routine will not be able to locate the right translation. Thus, a local minimum will then be selected as the absolute one.

In order to avoid this issue, the grid refinement process was eventually abandoned. Thus, the results in the remaining of the thesis are based on *Match* set to use one single cycle, with a fine ($N=150$ if not otherwise specified) grid.

Robustness of the result

Subsequently, a test was performed to check the robustness of the output when the input is slightly changed. In order to do that, the red section in fig 3.10 (upper

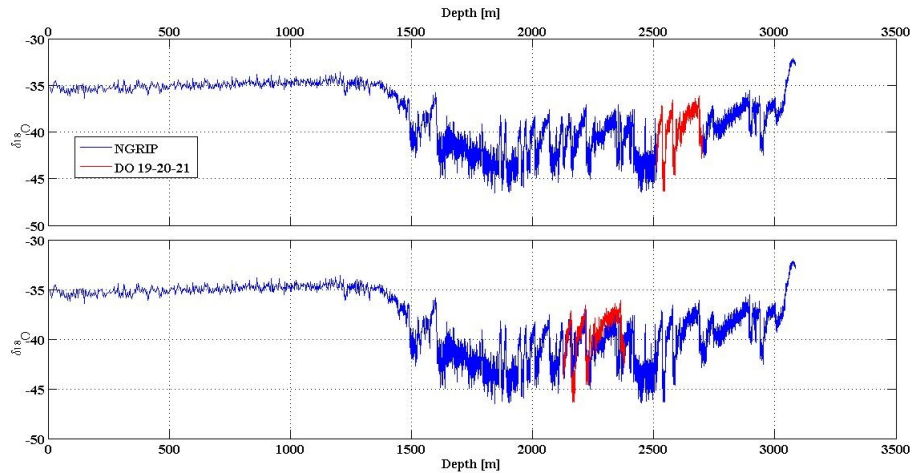


Figure 3.10: Example of a mismatch when the \mathcal{N} vector is poorly defined. The upper panel shows NGRIP $\delta^{18}\text{O}$ profile (blue) and a selection of it: DO 19-21 (red). The lower panel shows the mismatch setting $N=50$ in *Match*.

panel) is iteratively enlarged including one more data point at each boundary. Using NGRIP data, this corresponds to add $\sim 12\text{cm}$ on both left and right side of the selected area before performing the match. Such a minor change in the input should not affect the routine, which should estimate about the same translation and scale factors.

The result of such test is numerically shown in table 3.5. *Match* was set to perform only one cycle with $N=200$. The first two columns are the initial and final x values of the selected area y_2 ; the last two are the scale and translation factors best aligning y_2 to y_1 (original NGRIP $\delta^{18}\text{O}$ profile). The first row corresponds to the selection in fig 3.10 (upper panel).

In this test, a perfect match is given when $x_i \equiv dx$ and $s \equiv 1$. From table 3.5 it is visible that the discrepancy between x_i and dx is usually smaller than 1m; the estimated scale factor is even more precise. Thus, it is possible to conclude that the output of the algorithm is robust respect to slight changes in the input functions.

\mathbf{x}_i (m)	\mathbf{x}_f (m)	s	\mathbf{dx} (m)
2510.04	2690.07	0.97	2511.59
2509.92	2690.33	0.97	2511.26
2509.80	2690.59	0.97	2510.94
2509.69	2690.86	0.97	2510.61
2509.57	2691.13	0.97	2510.27
2509.46	2691.40	1.00	2509.94
2509.35	2691.67	1.00	2509.61
2509.24	2691.92	1.00	2509.30
2509.13	2692.16	1.00	2509.00
2509.01	2692.40	1.00	2508.69
2508.90	2692.63	1.00	2508.39
2508.78	2692.86	1.00	2508.09
2508.67	2693.09	1.00	2507.80
2508.55	2693.32	1.00	2507.50

Table 3.5: Robustness of the algorithm’s output. The rows are different matches, performed with one cycle and $N=200$. The first two columns are the boundary values of y_2 ; the third and forth are the scale and translation values which best align y_2 to y_1 .

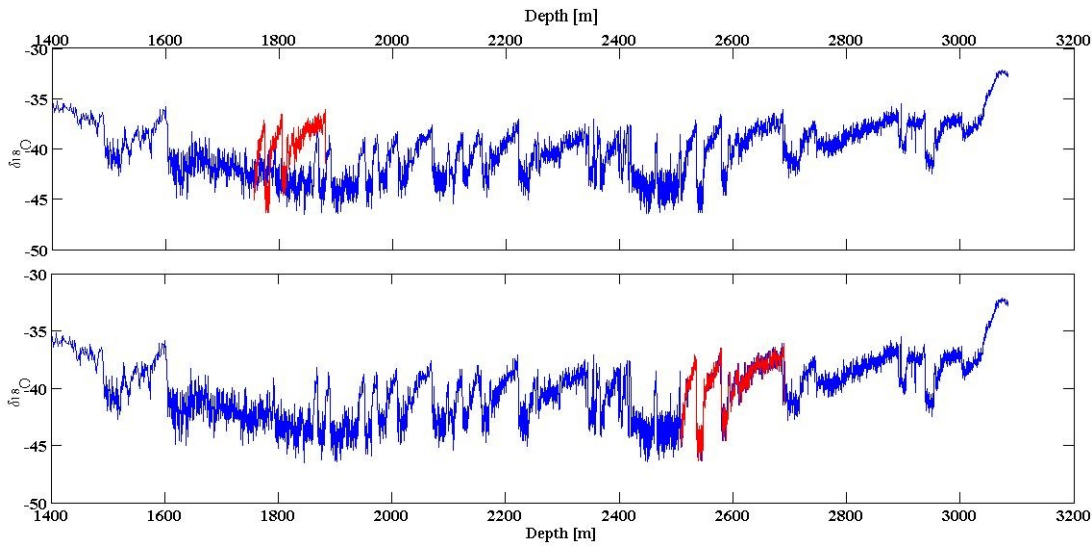


Figure 3.11: Simple test performed on the *Match* algorithm in order to check its reliability. A section of the NGRIP record (blue) is translated and rescaled (red, upper panel). The output of the routine is shown in the lower panel.

Test run

Finally, a test run is performed. The DO events 19 to 21, are rescaled and translated to create y_2 . This function, together with the original NGRIP profile y_1 , is given as input to *Match* (fig 3.11, upper panel). The result is shown in the lower panel.

In order to better understand how the whole *Match* routine works, a simple video is shown in fig 3.12. The input functions are the same as in fig 3.11: y_1 is the original NGRIP profile from $\sim 1400\text{m}$ depth to bedrock and y_2 is the DO 19-21 section (upper panel, blue and green respectively). The lower left panel shows the input functions in the Cartesian space. Black dots represent the translation factors dx_i (only four in this simple example); for each of them, y_2 is translated correspondingly and all the possible scale factors are applied (the green function stretches as s changes). The red circle highlights which dx is being used. For each (dx_i, s_j) pair, the log transform is taken respect to dx_i and the functions are interpolated on a common grid (lower

(Loading Circle-m-increase3.mp4)

Figure 3.12: Video showing how the *Match* algorithm works. Details in the text.

right panel), before the squared difference formula 3.9 is applied.

Chapter 4

The reference profile

The previous chapter described in details all the logical steps of the *Main* program. The core of the routine lies in the *Match* block; this algorithm estimates the translation and scale factors to be applied to a given input function f_2 in order to best align it with another function f_1 . The f_2 profile is any possible configuration created by the *Operations* block once an arbitrary number of breakpoints is set on the folded data. Thus, the method works by comparisons and the function f_1 is the reference profile.

4.1 A Greenland profile of the Eemian

In the problem at hand, such a profile would be a data sequence covering the Eemian with undisturbed stratigraphy. As described in chapter 2, none of the ice records in Greenland show MIS-5 with intact chronology. Landais et al. (2003) before and Suwa et al. (2006) later, proposed a reconstruction of the disturbed sections of ice at Summit. However, their studies were based on the analysis of ~ 80 samples for each core and the proposed reconstructions are too discontinuous to be used in this work. As a consequence, a reference function has to be searched in Antarctica, where this period is not corrupted by, e.g., flow disturbances or non-flat bottom topography.

Comparison of data profiles between the northern and southern hemispheres is not straightforward. The most reliable tool are atmospheric trace gases whose lifetimes well exceed the inter-hemispheric mixing. In principle this requirement should ensure that the concentration of the compound will be the same in every record thus allowing direct comparison, although some corrections may be needed. Methane, for example, is an appropriate candidate, being its residence time in the atmosphere ~ 10 years. Nonetheless, a slight scaling has to be introduced in order to correct for the inter-polar gradient (+5-7% south to north) due to different amount of sources between the hemispheres Chappellaz et al. (1997).

However, this thesis is based on stable isotopes data whose profiles cannot be compared directly. The temperature anomaly reconstruction in Greenland, inferred by the $\delta^{18}\text{O}_{ice}$ profiles, shows a total of 25 abrupt DO events characterized by warmings of 8-16 °C (NGRIPmembers et al., 2004; Lang et al., 1999). Antarctic ice cores, instead, do not show such rapid and large fluctuations. In fact, the corresponding events appear more smooth with typical amplitudes of 1-3 °C (Jouzel et al., 2007) and different timing respect to Greenland.

The difference in the isotopic ratios can be explained by the so called *bipolar seesaw* effect (BS), first introduced by Broecker in 1998. The meridional overturning circulation (MOC) is the process at the basis of the BS ,and it couples the northern and southern hemispheres in a complex way. The MOC in the Atlantic sector transports heat northward thus cooling the Southern Ocean. i.e. the waters encircling Antarctica at $\sim 60^\circ$ latitude. If the MOC was slowed down or totally switched off, no more heat would be advected northward; the result would be a cooling in the northern hemisphere and therefore a warming in the south. This simple concept implies an anti-phase relation between north and south (Broecker, 1998), meaning that a change in the MOC strength have opposite responses in the two cases. Stocker and Johnsen (2003) improved this model by coupling the original BS to a heat reservoir

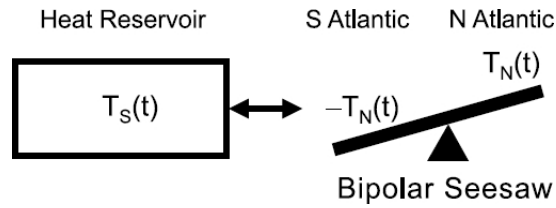


Figure 4.1: Schematic of the thermal bipolar seesaw model. The original BS is coupled to a heat reservoir representing the Southern Ocean. After Stocker and Johnsen (2003).

(thermal BS), as shown in fig 4.1.

According to their model, the southern heat reservoir evolution is given by:

$$\frac{dT_S(t)}{dt} = \frac{1}{\tau} [-T_N(t) - T_S(t)] \quad . \quad (4.1)$$

By the use of the Laplace transform, the solution of T_S can be written as:

$$T_S(t) = -\frac{1}{\tau} \int_0^t [T_N(t-t') e^{-t'/\tau}] dt' + T_S(0) \quad . \quad (4.2)$$

Therefore, T_S is a convolution of the temperature of the northern hemisphere with timescale τ . This parameter is the ventilation time of the southern reservoir, i.e. the time it needs to adjust to a given forcing responding by thermal inertia. Using this simple energy balance model, Stocker and Johnsen (2003) were able to produce a synthetic record of Antarctic temperature giving Greenland temperatures as input. Their reconstruction best fits observed data when the ventilation time of the Southern Ocean was set in the range 1000-1500 yr.

Siddall et al. (2006) first attempted to estimate northern temperature variability as a function of T_S and its derivative by inverting eq. 4.1:

$$T_N(t) = -T_S(t) - \tau \frac{dT_S(t)}{dt} \quad . \quad (4.3)$$

By the use of this inverse thermal bipolar seesaw model, they reconstructed the temperature evolution in Greenland during the last four glacial cycles. However they concluded that this model did not produce reliable results during interglacial periods.

This result is in line with the following observation. The thermal BS model was derived to explain the difference in temperature variability across the two hemispheres specifically during the last glacial and over millennial timescales. Interglacial periods, whose variability is most likely a combination of different factors (e.g. solar changes, greenhouse gases and albedo feedbacks) on Milankovitch timescales, are not meant to be reproduced by this simple model (Stocker and Johnsen (2003) and references inside).

The first reconstruction of Greenland temperature variability beyond the present limit of 123 Kyr BP (NGRIP) and including interglacial periods was produced by Barker et al. (2011). In their study, they used stable isotopes data from GISP2 (Greenland) and EDC (EPICA¹ Dome C, Antarctica). They proceeded by performing a lead/lag analysis between the high-pass filtered Greenland and Antarctic profiles $GL_T\text{-hi}$ and $AA_T\text{-hi}$, where the prime denotes the derivative. They observed a near-zero anti-correlation between the two curves. Building on this result, they assumed that the Antarctic rate of change in T and the Greenland temperature anomaly are inversely proportional.

Their approach is essentially similar to the work of Stocker and Johnsen (2003), with one difference. They do not connect the time derivative of AA_T with the temperature difference between the reservoir and the southern end of the seesaw (4.1). Instead, they relate it directly to the northern temperature anomaly GL_{T^*} . Moreover, in their reconstruction they include the Milankovitch timescale variability in order to be able to reproduce a correct signal for the last eight glaciations back to 800 Kyr BP. Eventually, their profile is given by the combination of the low and high variability synthetic records:

$$GL_{T\text{-syn}} = GL_{T\text{-syn}_{hi}} + GL_{T\text{-syn}_{lo}} \quad . \quad (4.4)$$

The high variability profile is estimated by $AA_T\text{-hi}$; the orbital timescale component, instead, is simply the Antarctic one shifted 2000yr towards younger ages. Both are

¹European Project for Ice Coring in Antarctica

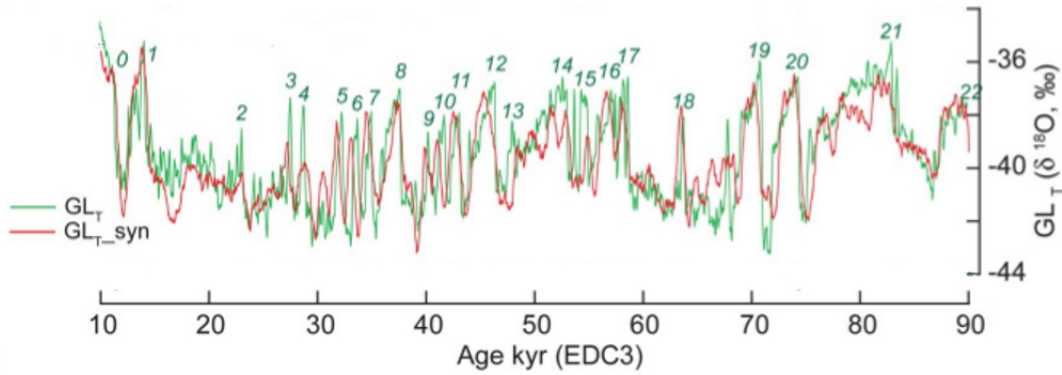


Figure 4.2: Synthetic reconstruction of Greenland temperature variability ($GL_{T\text{-syn}}$, red curve) compared to GISP2 $\delta^{18}\text{O}$ profile (GL_T , green curve) tuned to EDC3 via methane. Numbers identify the Dansgaard-Oeschger events. After Barker et al. (2011).

then rescaled to GISP2 values:

$$GL_{T\text{syn}_{hi}} = \frac{AA_{T\text{-hi}}'}{\sigma(AA_{T\text{-hi}}')} \sigma(GL_{T\text{-hi}}) \quad (4.5)$$

$$GL_{T\text{syn}_{lo}} = \frac{AA_{T\text{lo}} - \langle AA_{T\text{lo}} \rangle}{\sigma(AA_{T\text{lo}})} \sigma(GL_{T\text{lo}}) + \langle GL_{T\text{lo}} \rangle \quad (4.6)$$

where $\langle \cdot \rangle$ and $\sigma(\cdot)$ denote the mean and standard deviation. The low variability profiles are obtained applying a 7000 yr running mean on the original records.

Fig 4.2 shows their synthetic profile $GL_{T\text{-syn}}$ compared to GISP2 data (GL_T) between 10-90 Kyr BP; the numbers refer to the DO events in Greenland. Even if the match between the two curves is not perfect, their reconstruction captures quite precisely the variability of the original record.

In this thesis, the method from Barker et al. (2011) was reproduced. The result can be appreciated in fig 4.3; the original data series is plotted in green, while the reconstruction is given in blue. The comparison between the two curves shows general agreement. Nevertheless, the blue line deviates from the green both in amplitude and timing of the events. The latter issue is more visible in fig 4.4, where only the first 140 Kyr of the two reconstructions are plotted.

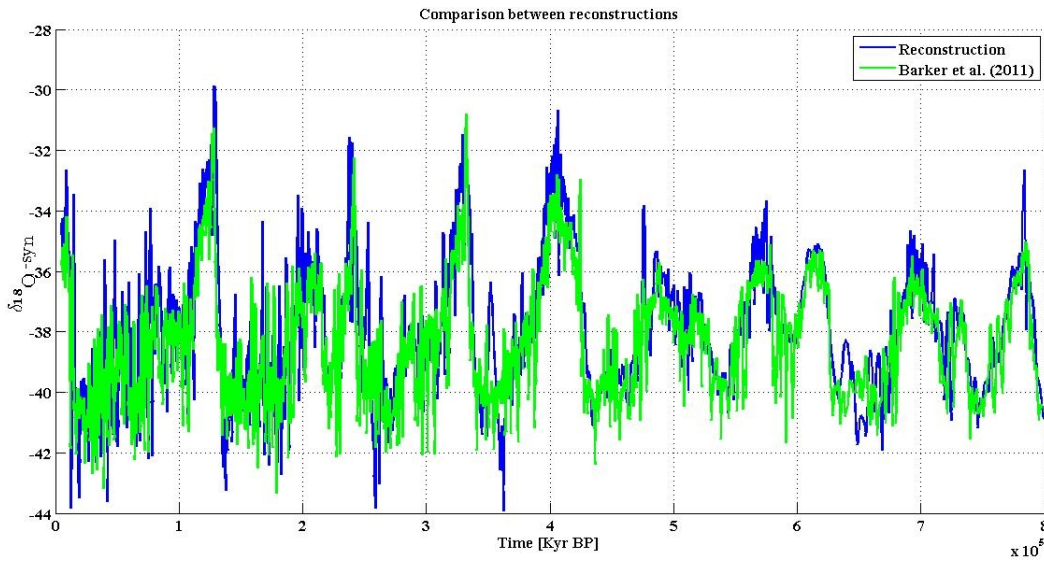


Figure 4.3: Comparison between Barker et al. (2011) synthetic Greenland profile (green) and reconstruction of their method (blue). Each curve on its time scale (see details in the text).

The time lag between the profiles probably lies in the fact that Barker et al. (2011) have tuned GISP2 and EDC via methane, while this work used GISP2 on its original timescale.

The amplitude difference is related to the GISP2 time window used in the method. This can be seen in eq 4.6, where the mean value of GL_{T-lo} is imposed on the normalized function. This average value is strongly influenced by the amount of Holocene 'warm ice' included in the calculation. The more is included, the 'warmer' will be the resulting reconstruction. In fig 4.3 and 4.4, the green function is calculated using GISP2 data in the 5-100 Kyr BP range.

Moreover, one more source of discrepancy between the two profiles is given by the 2000 yr shift they apply on the low variability curve. In fact, being different the two timescales, this may contribute to the mismatch.

Despite the general resemblance between the two curves in fig 4.3 and 4.4, it was decided to use directly the original data from Barker et al. (2011) in the remainder

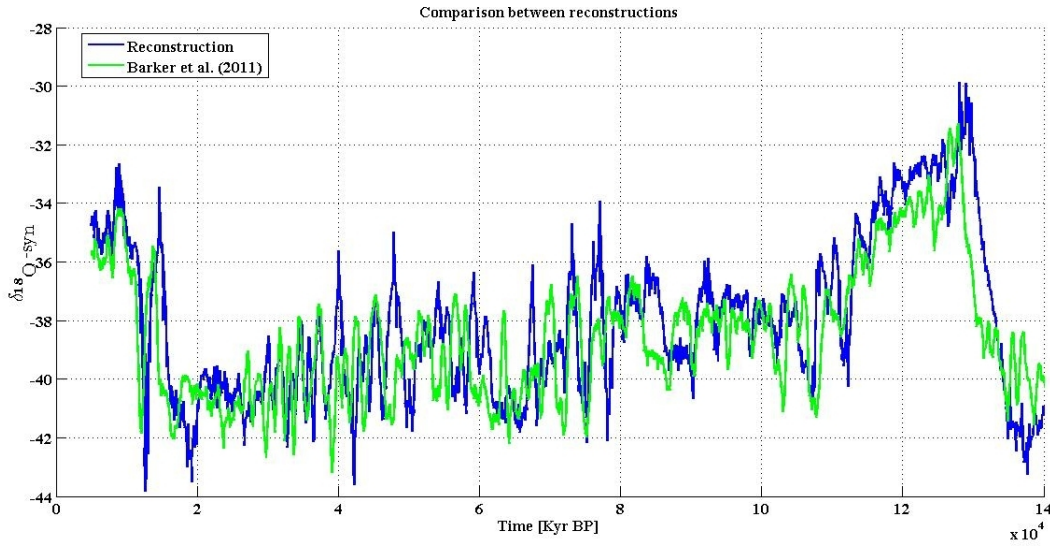


Figure 4.4: Detailed view of the first ~ 140 Kyr of the two profiles in fig 4.3.

of the thesis. In this way, any error introduced by the reconstruction of the method can be ignored.

From time to equivalent depth

Since the profile from Barker et al. and colleagues is a reconstruction, it was derived directly on a time scale. However, sections of ice whose stratigraphy is disturbed are naturally available on a depth scale only. In order to correct for that, the \mathcal{S} domain in the *Match* routine could be set to cover different orders of magnitude. However, a different approach is chosen.

A conversion is performed on the GL_T profile, in order to transfer the time array to an equivalent depth vector. In principle, such a conversion can be applied easily. Be D the length of an ice core, T the time range it covers and \bar{T} its temporal array. Then, the equivalent depth vector \bar{D}_{eq} can be estimated as:

$$\bar{D}_{eq} = \bar{T} \cdot \underbrace{\frac{D}{T}}_{\alpha} \quad . \quad (4.7)$$

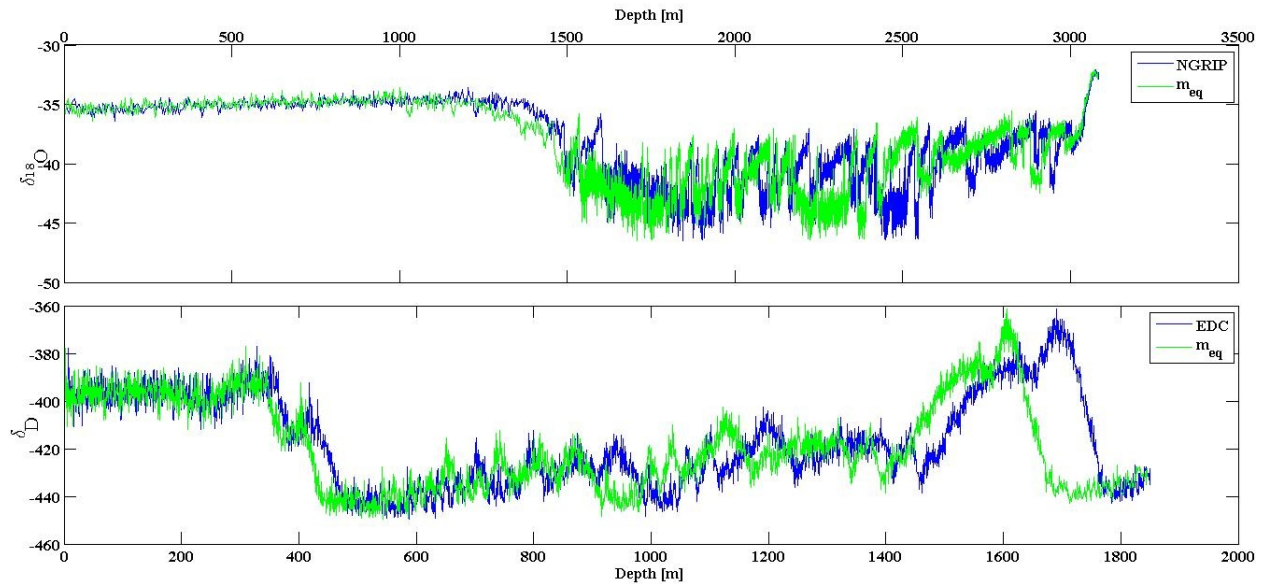


Figure 4.5: (Top panel) Comparison between the NGRIP record versus the original depth (blue line) and the equivalent depth (green). (Bottom panel) Same for the EDC record.

However, this simple expression implies that the factor α between depth and time is constant throughout the length of the core, or the history of the archive. Such an assumption would be wrong.

An improved conversion can be achieved if the length D is divided in sub-intervals and the above equation is calculated separately on every section. Eq 4.7 would then become a summation over all these intervals with different α factors. In fig 4.5 an example of this method applied on NGRIP and EDC data is shown. In both cases only two different α values were used, the former for the Holocene period and the latter for the glacial. The profiles in green are plotted respect to the estimated equivalent depths.

Since the *Match* algorithm includes a calculation of the scale factor between the two input curves, it is not necessary to achieve a more detailed precision at this stage. The reconstruction from Barker and colleagues (cropped at ~ 140 Kyr BP or ~ 3300 m eq. depth) is plotted against its equivalent depth in fig 4.6 (green function).

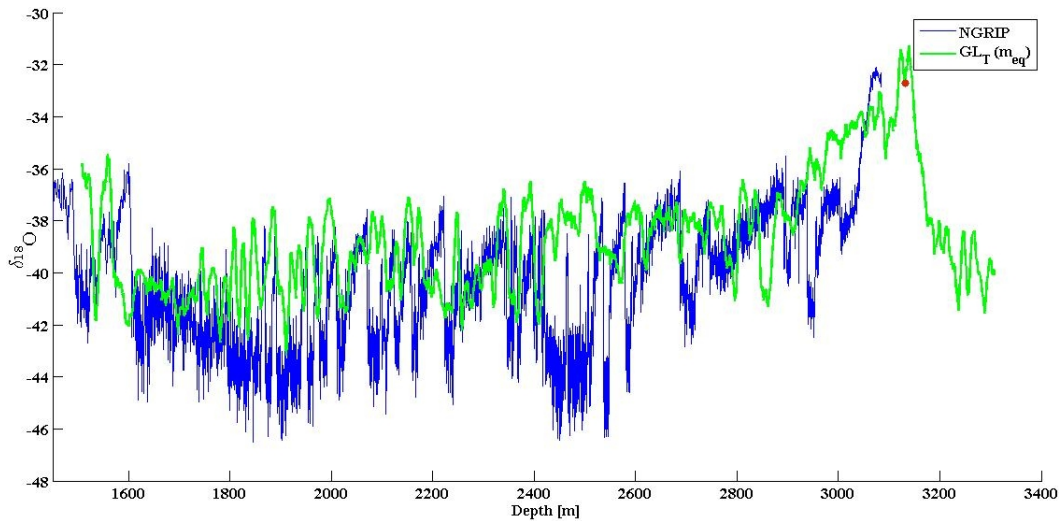


Figure 4.6: Reconstruction from Barker and colleagues cropped at ~ 140 Kr BP converted to equivalent depth (green line). Also shown the NGRIP profile versus its original depth. The red dot indicates the merging point (see text in the next section).

Also shown for comparison is the NGRIP profile on its original depth scale.

A combination between NGRIP and GL_T

As explained above, the GL_T profile is a synthetic record of Greenland variability estimated from Antarctica by inverting the thermal bipolar seesaw model. Even if the match with respect to the GRIP core (and other records) showed good agreement, it is a safer choice to use real data where they are available.

The NGRIP ice core can be used for this scope since it extends back to ~ 123 Kyr BP, covering the last ~ 7 Kyr of MIS-5e. Furthermore, the use of such record permits to avoid including the end of the GL_T Eemian, whose high variability (not mirrored at NGRIP) might be an artifact due to the differentiation process used in the reconstruction.

A complete Eemian section can thus be created by prolonging NGRIP further back by the use of the GL_T reconstruction. Simply plugging the two records at 123 Kyr

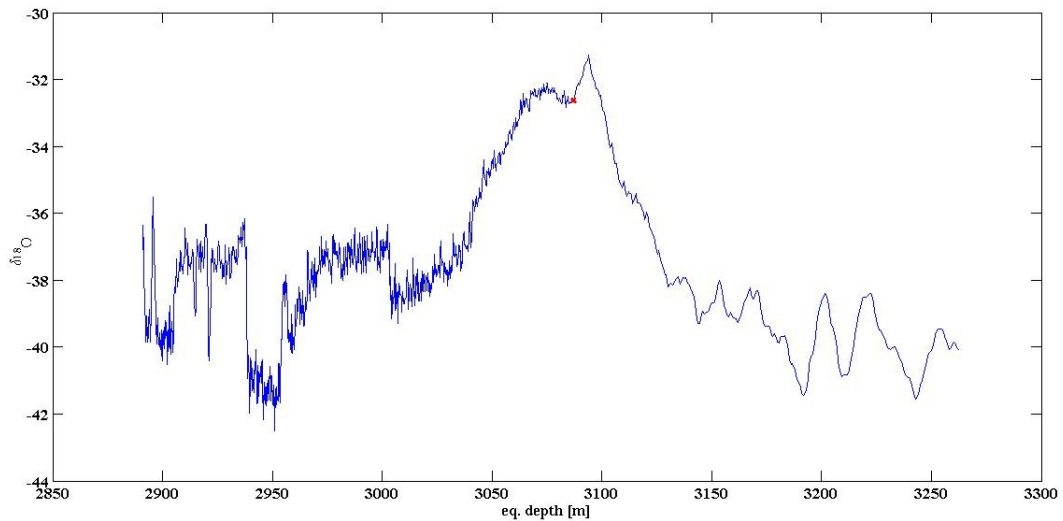


Figure 4.7: Combined reconstruction of the $\delta^{18}\text{O}$ profile during the Eemian period. The red dot indicates the merging point between the NGRIP data (left) and the GL_T reconstruction (right).

BP corresponds to connect the two curves at about 3100m depth in fig 4.6, thus generating an Eemian section characterized by two sharp peaks divided by a pronounced trough. Such a reconstruction looks unlikely. Therefore, it was decided to complete NGRIP with GL_T from 3130m depth to $\sim 3300\text{m}$ in fig 4.6, where the isotope values are on the same level. The resulting profile is thus shown in fig 4.7, the red dot indicating the merging point (accordingly, a red dot is also shown in fig 4.6).

Such a choice is somewhat arbitrary. Nevertheless, it should be noted that the two records are not synchronized, NGRIP being on the GICC05modelext and GL_T being derived by EDC on the ecd3 time scale. Therefore, there might be a time offset between the two data series. Moreover, it was observed that the precise location of the link between the two records did not vary much the output of the simulations, provided the absence of a marked trough during MIS-5e.

Furthermore, the isotopic ratios of the two records might need some corrections before generating the combined record. In fact, the approach above does not consider differences in conditions at different locations such as, e.g., the altitude or atmospheric

circulation patterns. These factors influence e.g. the temperature and accumulation rate at the site, thus affecting the isotopic ratio.

However, the reconstruction in fig 4.7 provides a first order estimate of the $\delta^{18}\text{O}$ profile in Greenland during MIS-5e, useful for the exercise of this thesis.

Chapter 5

Results

The results of this work are divided into three categories. (1) The *Match* algorithm is used in order to semi-automatically align data from two different ice cores; (2) the *Main* routine is applied on synthetic folded data; (3) a combination of the two is used on real folded data from NEEM, GRIP and GISP2 disturbed sections.

5.1 Semi-automatic match between NEEM unfolded section to NGRIP

As explained and shown in chapter 3, the *Match* algorithm permits to align two given functions by estimating the best translation and scale factors between the inputs. This routine represents a powerful tool. In fact, it can be used to automatically register two given data profiles. This fact also implies that a data series can be automatically dated, assuming the other one has already a known time scale.

It should be specified that such algorithm cannot, and is not intended to, replace the actual dating process, based on different combined analyses such as, e.g., visual stratigraphy, ECM (electric conductivity measurements) and CFA (continuous flow analysis), together with the use of temporal horizons given by volcanic ash in layers.

5.1. SEMI-AUTOMATIC MATCH BETWEEN NEEM UNFOLDED SECTION TO NGRIP71

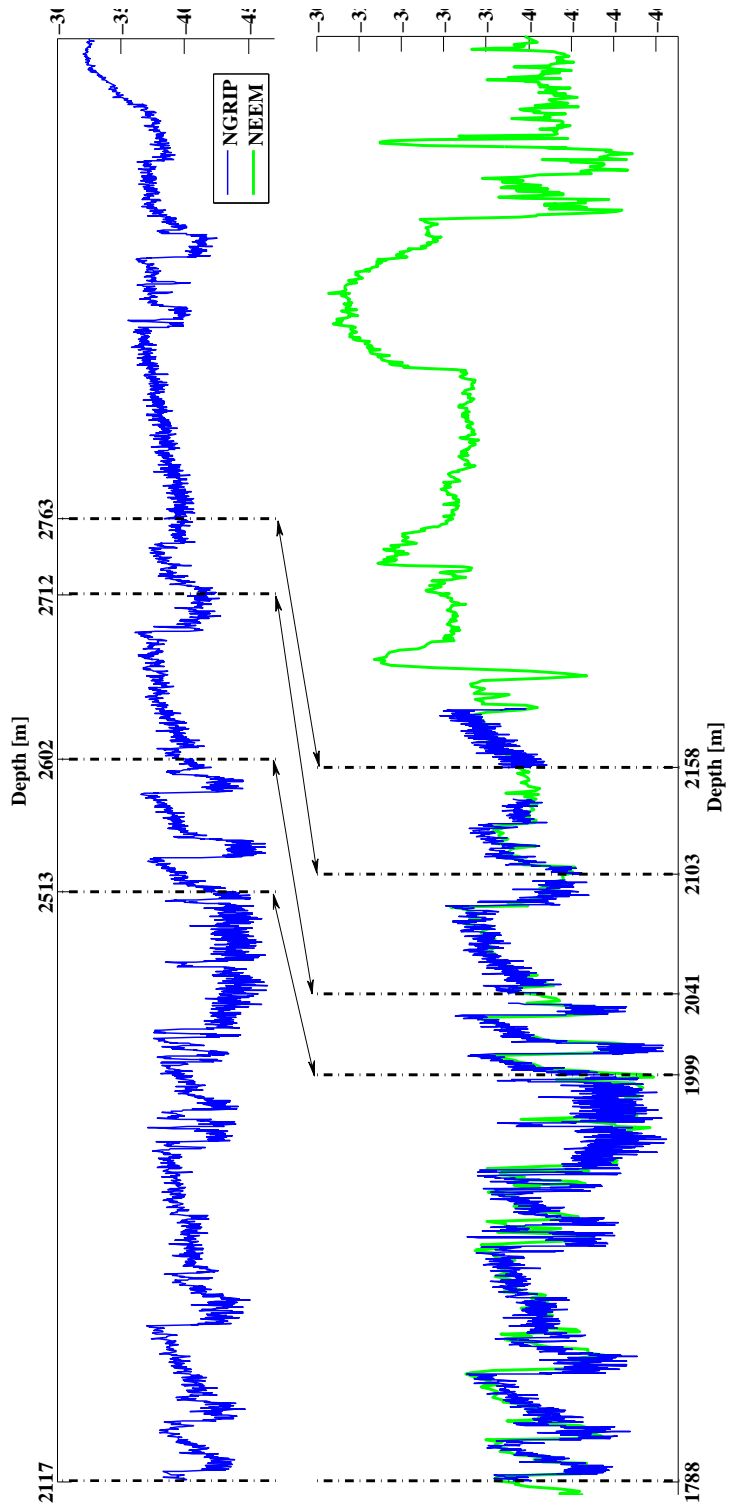


Figure 5.1: Semi-automatic match between NGRIP (blue) and NEEM (green) $\delta^{18}O$ data series. The NGRIP profile is divided into five sections. The vertical black lines identify the initial value of each section. The scale and translation factors applied to the intervals are given in table 5.1. Specifics of *Match* are: $N \times S = 150 \times 50$; $S = [.2, 2]$.

	x_i (m)	x_f (m)	s	dx (m)
1	2117.49	2510.04	0.53	1788.21
2	2512.54	2591.91	0.47	1998.78
3	2601.63	2711.45	0.53	2040.99
4	2712.41	2762.84	0.77	2102.77
5	2763.22	2894.32	0.23	2158.18

Table 5.1: Initial and final x values (first and second columns) of the five NGRIP sections (rows) matched to the NEEM $\delta^{18}\text{O}$ profile. The scale and translation factors applied to each section are listed in the third and fourth columns.

Nevertheless, it can give a first estimate for the dating of a new record in a very limited time (typically, a few seconds).

Therefore, *Match* was used to perform the alignment between NGRIP and NEEM $\delta^{18}\text{O}$ profiles, where the two data series are not visibly different, i.e. above $\sim 2890\text{m}$ and $\sim 2200\text{m}$ depth, at NGRIP and NEEM respectively. The output of the program can be appreciated in fig 5.1.

NGRIP data between approximately 2100m and 2890m depth were split into five parts. The initial x_i and final x_f boundaries of these sections are listed in table 5.1 (first and second columns). The black dashed lines in fig 5.1 mark the initial values of the intervals.

Each section was then translated and rescaled by *Match* in order to automatically produce the best alignment respect to the NEEM profile. The scale and translation factors applied to the intervals are given in table 5.1, on the third and fourth columns respectively¹. The resolution of the search space was $N \times S = 150 \times 50$ and the \mathcal{S} domain spanned the $[.2, 5]$ interval. Each comparison lasted for about ten seconds.

¹The translation factor is given according to equation 3.7. Therefore the quantity dx expresses the new initial value respect to NEEM depth.

It was necessary to divide the 2100-2890m NGRIP section into five separate pieces because the algorithm applies the scale factor uniformly on the input functions. Therefore, if different sections of the first profile have different scaling respect to the second, they have to be divided and separate comparisons must be performed. In this perspective, the alignment was semi-automatic as the different sections had to be identified manually.

The application of *Match* to the five selected sections of NGRIP and NEEM aligned the two records quite precisely. The total amount of computational time needed for the alignment is about a minute. Since the NGRIP ice core was dated by the use of different parameters such as the ones mentioned above, temporal constraints can be set on the NEEM data between $\sim 1780\text{m}$ and $\sim 2200\text{m}$ depth. According to the GICC05modelext, this depth interval roughly covers the 40Kyr to 100Kyr time period (Vinther et al., 2006; Rasmussen et al., 2006; Andersen et al., 2006; Svensson et al., 2008; Wolff et al., 2010).

5.2 NGRIP: synthetic folded data

Once the performance of the *Match* algorithm was tested in several ways, the last being the alignment of NEEM to NGRIP down to $\sim 2200\text{m}$ depth, it was possible to proceed on applying the *Main* program on the corrupted data sections at NEEM, GISP2 and GRIP.

Prior to doing so, it was decided to test the whole routine by the use of synthetic folded data. In order to do that, a program was developed, which permits to corrupt a given input function (NGRIP in the test). This program has a graphical user interface (GUI) for improving usability and quickening the process of creating any preferred disturbed profile.

In fig 5.2, an example is given. In the panel on the left, the original NGRIP $\delta^{18}\text{O}$ profile is plot on the GICC05modelext time scale. The user can set an arbitrary

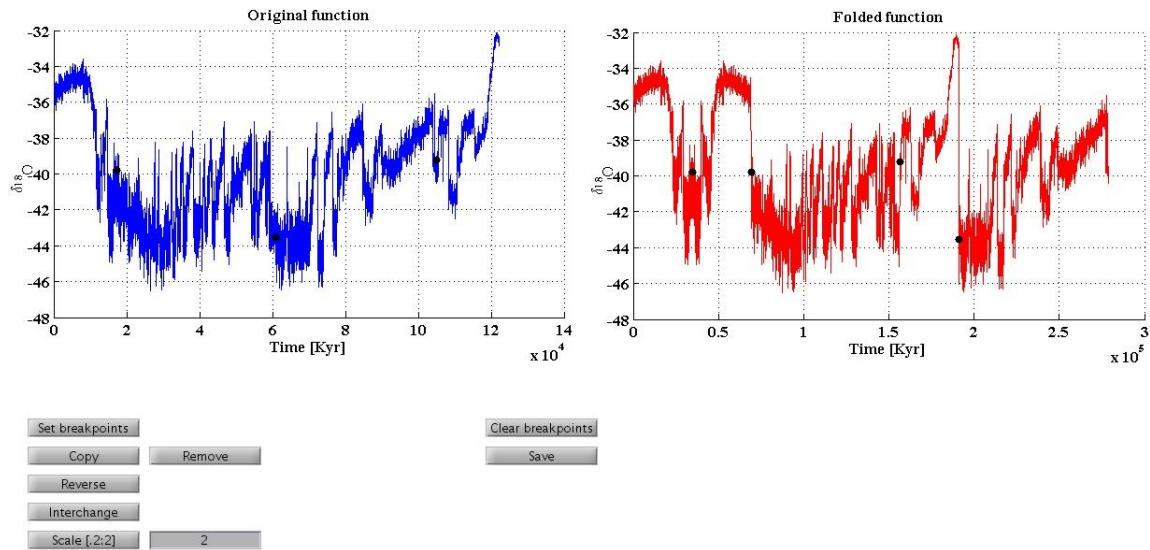


Figure 5.2: Generation of a corrupted version of the NGRIP $\delta^{18}\text{O}$ profile (blue line). The first interval is copied and reversed, the last two are interchanged. Moreover, an arbitrary scale factor is applied on the folded signal.

number of breakpoints simply by clicking on the graph at the preferred positions (black dots). All the other options work in the same graphical way. Once the intervals are created, it is possible to apply all the operations as in the *Operations* routine described in chapter 3. Moreover, a given section can be erased and a scale factor can be applied on the whole function. The plot on the right panel shows the folded signal, which updates automatically at every change. In the example in fig 5.2, the first interval is copied and reversed and the last two are interchanged. Moreover a global scaling $s=2$ is applied to the function. At last, the synthetic corrupted profile can be saved for further use or modification.

Once a disturbed NGRIP profile is created, the *Main* program can be applied in order to test whether it is able to recover the correct sequence. As explained in chapter 3, the logical steps of the routine are: *Splitting - Operations - Match*. The first phase is very important. In fact, the position of the breakpoints influence

the final outcome of the whole program. In order to better simulate a real situation, *Main* was run several times, with breakpoints set increasingly further away from their original positions. Thus, it was possible to test whether the algorithm is able to retrieve the correct profile even after the introduction of this error. In this test the original NGRIP $\delta^{18}\text{O}$ data are used as the reference profile in the *Match* algorithm.

Fig 5.3 shows a folded version (green) of the NGRIP record (blue). The black dots and vertical lines in the upper panel identify where the original record was broken. The disturbed signal (green) is created by the use of three operations: removal of the first interval, inversion of the third one and interchange of the third with the second. Moreover, an arbitrary scaling is applied on such sequence.

Once the disturbed GRIP version was created, the *Main* program was run several times. In the lower panel, the positions of the breakpoints at each run are shown (dots). At the first run, their location is unchanged (black dots); in subsequent simulations, they are set at increasing distance from the original positions, randomly on the left or on the right (red dots). The lighter the shade, the bigger the offset with respect to the original position.

Therefore, the red dots show where the green profile was broken at each *Main* run. The gray bars, neighbourhoods of the black points, help the visualization. Each neighbourhood is 1 Kyr larger than the previous one. Thus, at the last simulation the green disturbed profile was broken at ~ 97 Kyr and ~ 109 Kyr, instead of ~ 91 Kyr and 115 Kyr respectively (black dots).

After the disturbed function is divided into intervals (*Splitting*), each simulation produces $\Pi=78$ candidate solutions, according to fig 3.2 with $n=3$ (*Comparisons*). Each of them is compared to the original NGRIP profile (*Match*), whose best scale and translation factors correspond to the minimum of the distance surface described in chapter 3.

Therefore, at last there will be 78 minima, one for each comparison. This is shown in fig 5.4 for the first simulation performed (black dots). The three panels separate

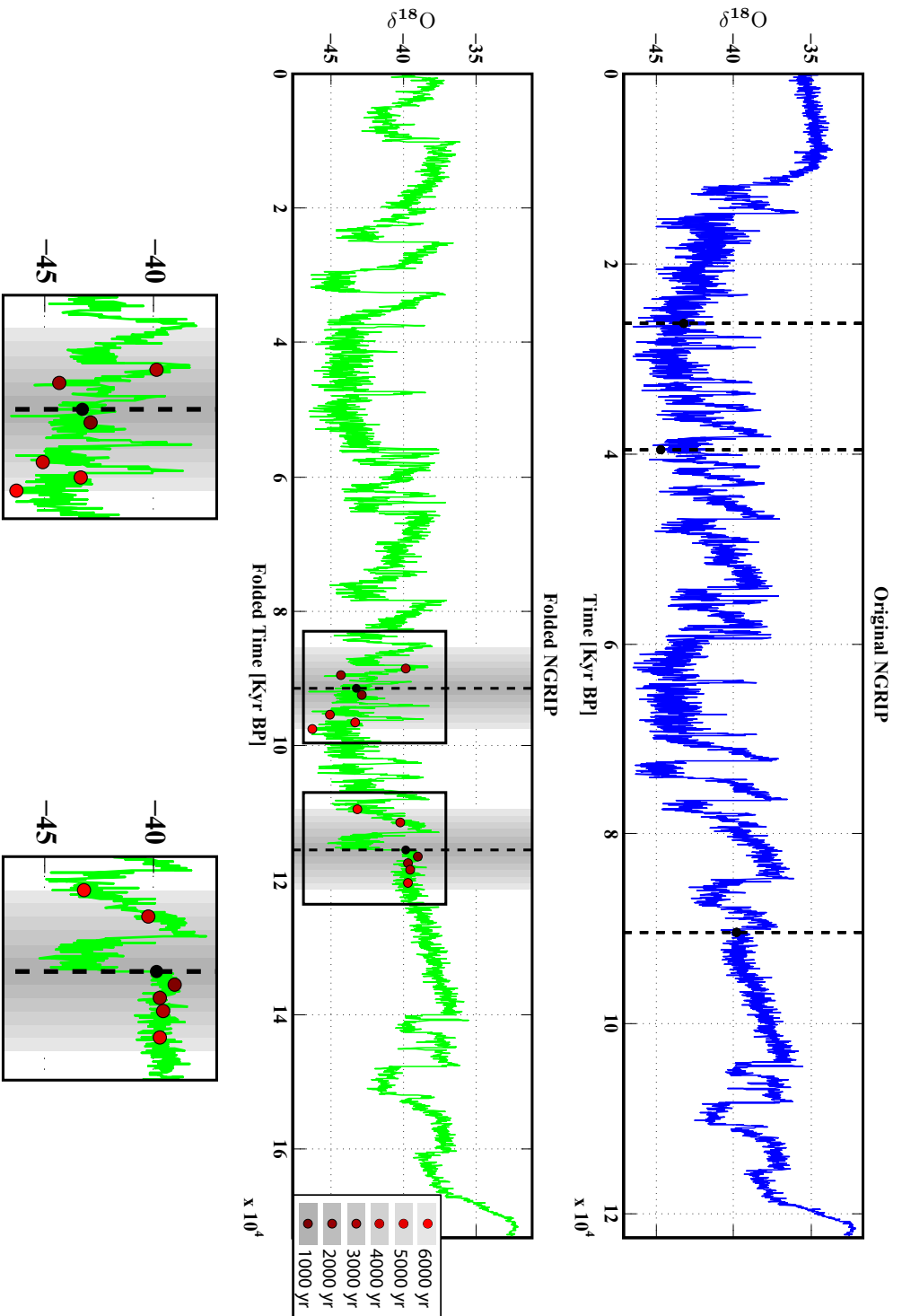


Figure 5.3: (Top panel) The original NGRIP profile (blue) is broken into four intervals I_k by the application of three breakpoints (black dots and lines). (Bottom panel) Disturbed NGRIP version (green) constructed by (1) the removal of I_1 , (2) the reversal of I_3 and (3) the swap of I_2 with I_3 . At last, (4) an arbitrary factor is applied on the green profile. The *Main* program is run several times, setting the breakpoint and increasing distance from the original positions (red dots). The shift is randomly positive or negative. The results of the simulations are given in fig 5.5.

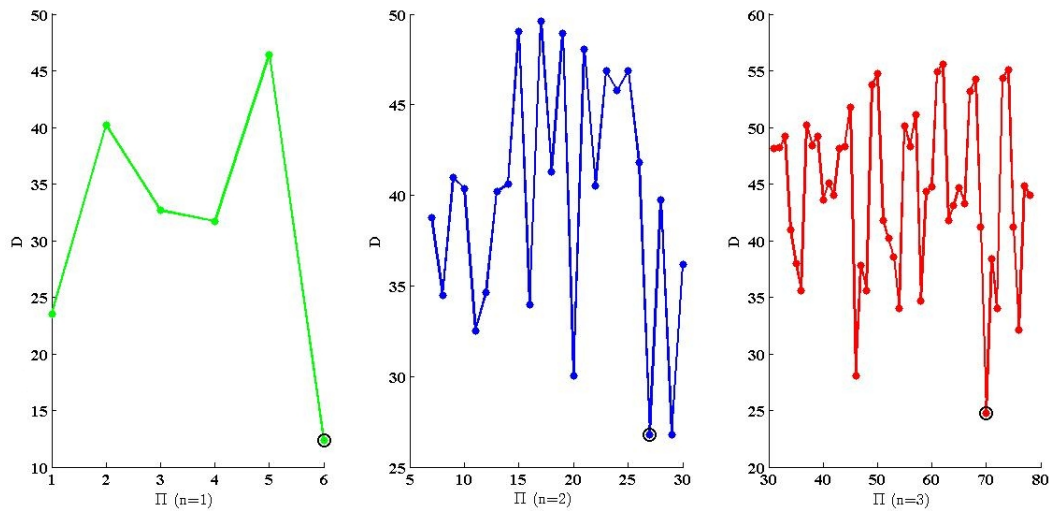


Figure 5.4: Minima of the 78 comparisons performed by the *Main* program for the first simulation (black breakpoints in fig 5.3 lower panel). The three panels cluster the configurations generated using only one interval (left), two intervals (center) or all (right). A black circle indicates the absolute minimum in each group.

the configurations built using only one interval (left), two intervals (center) and all of them (right). In each case the minimum of the corresponding section is highlighted by a black circle.

The results of the seven simulations are given in fig 5.5. Reconstructions are plotted in green; the original NGRIP data series is shown in blue. Each plot correspond to a simulation; the profiles shown are the best configurations, selected among the options built using all the three intervals $\Pi_{(n=3)}$ (see fig 5.4 right panel). A fully automated way of identifying the best solution was not achieved. In fact, the absolute minimum of the minima in fig 5.4 is always among the configurations generated using only one interval (left panel). The reason for this lies in the length of the function y_2 compared to the reference function y_1 . Imagine two fair alignments a_1 and a_2 , respectively belonging to $\Pi_{n=1}$ and $\Pi_{n=2}$; since a_1 is shorter, the sum of the squared differences will tend to be smaller than in a_2 . Therefore, a_1 will be

selected as best match even if a_2 aligns a longer stretch of the two functions.

If this was the only issue, separately selecting the absolute minimum of the n groups in fig 5.4 would be the solution. However, other particular situations may arise. One example is the following. Among the possible combinations, there will be one where the last interval was interchanged with the first one. In this case, the first part of y_2 will naturally match particularly well the last section of y_1 , while the remaining part will not be used in the calculation of D . Therefore, this configuration will most likely be selected instead of the one where the intervals are in the right order; in fact, this option, being longer, will probably have a higher D value.

In order to correct for this, a weighting function was created, which corrected the D values according to the portion covered in the reference profile. However, such approach did not increase the precision in selecting the best candidate solution and was therefore abandoned. Eventually, a manual control had to be performed. Nevertheless, this operation was required only after the selection of a few candidate solutions out of the 78 generated by the program ($n=3$).

Thus, for each run, the configurations corresponding to the five lowest minima among $\Pi_{(n=3)}$ were plot and the best was selected manually.

This procedure spotted the original sequence of data in every simulation but one, run number 3 in fig 5.5. At a close look, in fact, it can be seen that in this case the first part of the reconstructed profile (green) is reversed with respect to the original NGRIP. Nevertheless the main shape of the profile looks correct; this is a consequence of the first interval covering a quite short time period, so that it influences less when evaluating the squared difference.

In conclusion, under the assumption that the foldings are consistent with the idealized options used to corrupt the stratigraphy, this test proved that the *Main* program is robust and is able to retrieve the original data sequence. This it true even when the disturbed profile is not divided at the precise points where the corruptions were applied.

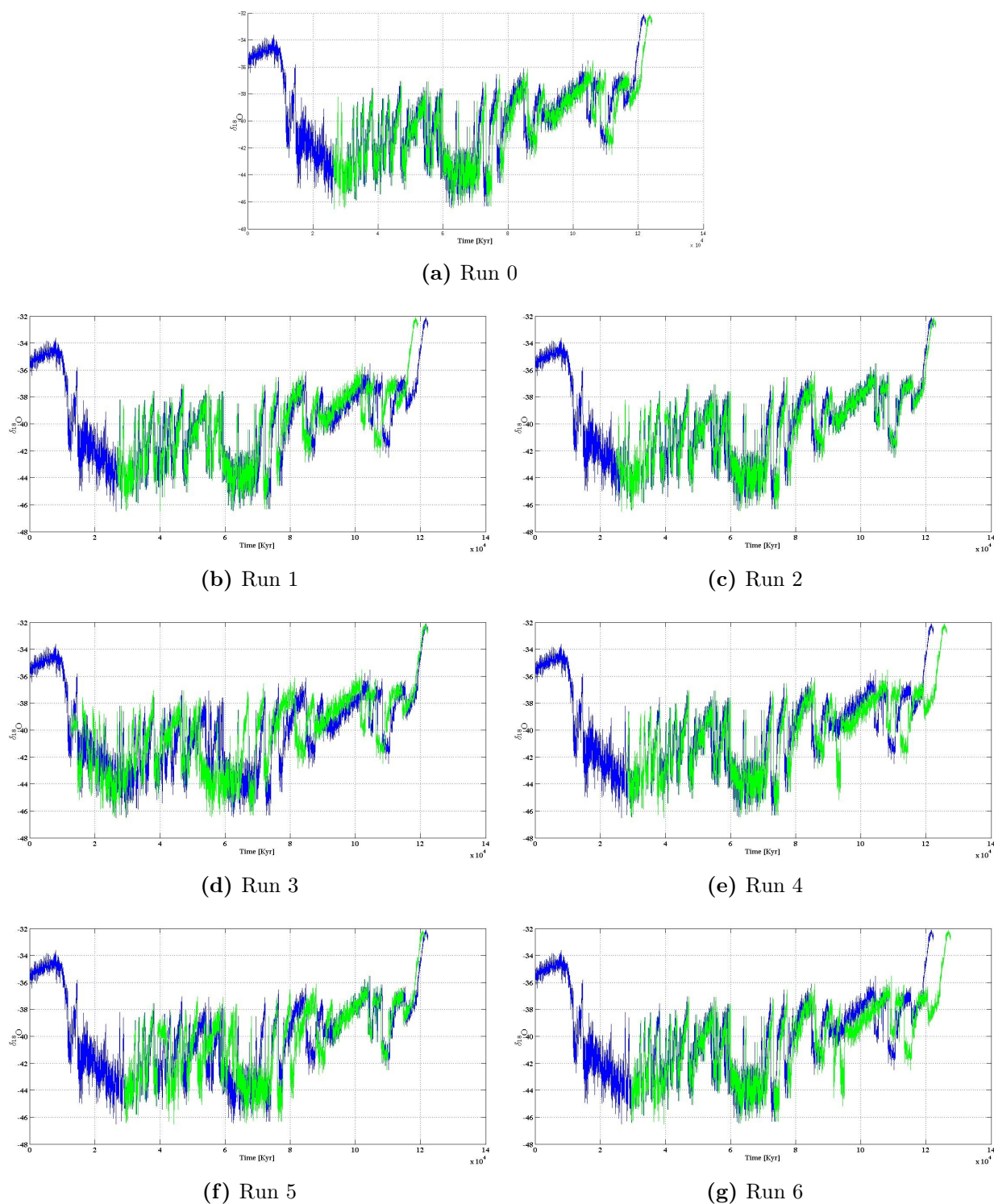


Figure 5.5: Results from the seven *Main* runs corresponding to different choices of the breakpoints in fig 5.3 bottom panel. From 0 to 6, the position's offset is iteratively increased by 1 Kyr (see 5.3 zoomed boxes).

5.3 Corrupted sections of ice at NEEM and Summit

Finally, the complete routine could be applied to real disturbed sections of ice at NEEM, GRIP and GISP2, in order to reorganize the data and try suggesting a chronologically plausible reconstruction of the Eemian period.

However, two important issues immediately arose. The first step of the *Main* program consists of setting an arbitrary amount of breakpoints in the data in order to divide the folded section into n intervals. However, it is not a priori determined where to position them. One option would be to check whether both the concentration of gases and the ratio between the stable isotopes abruptly change at the same depth. This would mark a possible disturbance. In fact, due to the firn densification process, there is an offset in age/depth between the quantities mentioned above. However, only $\delta^{18}\text{O}$ data were used in this work, preventing the possibility of using such approach. Therefore, no general method was applied while setting the breakpoints and the choice of their location will be justified singularly for each core in the following sections.

One more issue was the uniformity of the scaling inside the *Match* algorithm. This limit of the actual version of the routine prevents to capture the right answer if a non-uniform scaling is present. To avoid this problem, it was decided to use only part of the *Operations* block inside *Main*. More specifically, it was inhibited the call of *Interchange*. Thus, the configurations generated were simply the n intervals in which the original section was split, plus their inverted versions. This choice produced a very limited amount of candidate solutions, thus allowing to visually verify where they independently best fit respect to the reference profile generated in the previous chapter. Consequently, it was possible to check whether a combination of some specific intervals, after being rescaled and translated, might represent a chronologically consistent version of the Eemian period.

The simulations described in the next sections were all performed setting *Match* parameters to $N \times S = 250 \times 100$ and $\mathcal{S} = [.2, 5]$.

	\mathbf{x}_i	\mathbf{x}_f	\mathbf{s}	\mathbf{dx}
\leftarrow •	2212.10	2223.65	2.31	3038.32
• \rightarrow			0.77	3099.02
\leftarrow •	2263.80	2292.40	0.72	3038.22
• \rightarrow			0.36	3101.55
\leftarrow •	2367.20	2433.75	1.00	3041.50
• \rightarrow			0.80	3058.64

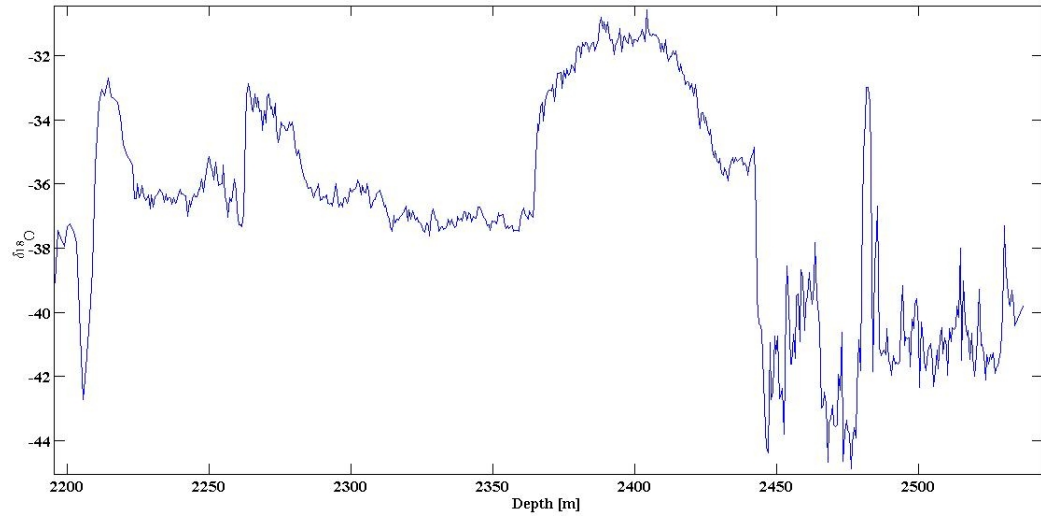
Table 5.2: NEEM. Boundaries (first two columns) of the selected intervals. The scaling and translation are given respectively in the third and fourth columns for both possible orientations (shown by the arrows).

NEEM

Among the Greenland ice cores whose deepest layers show a disturbed stratigraphy (NEEM, GRIP and GISP2), NEEM is most likely the record where the method developed in this thesis applies the better. In fact, its structure suggests that the foldings developed on a bigger scale rather than at Summit (see next section and discussion in chapter 6). The stable isotopes at NEEM do not show abrupt transitions from glacial to interglacial values in a narrow range of meters, as it is the case at GRIP and GISP2 sites. Instead, two rather long sections, visible in fig 5.6 before the dome structure, show a fair resemblance.

It is not unreasonable to hypothesize that these two sections are a copy of each other. Thus, the breakpoints were set accordingly, in order to test whether any interesting match can be highlighted by the program. If this conjecture is correct, the two sections should match the same region with respect to the reference profile.

The ~ 2210 - 2430 m range was selected for the simulation. The deepest part of the core was assumed to most likely belong to a period older than the Eemian. Fig 5.6b shows the selected section, together with the reference profile used in the *Match*



(a) Disturbed NEEM section

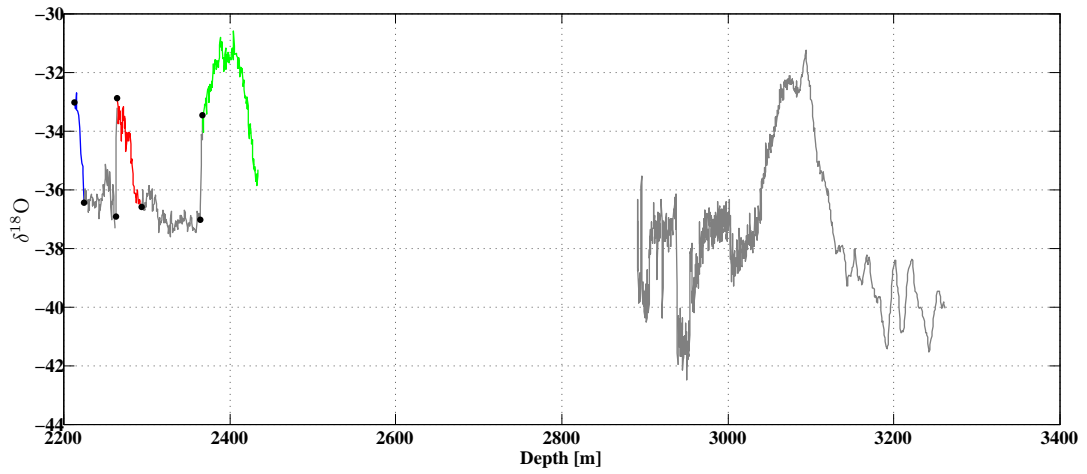
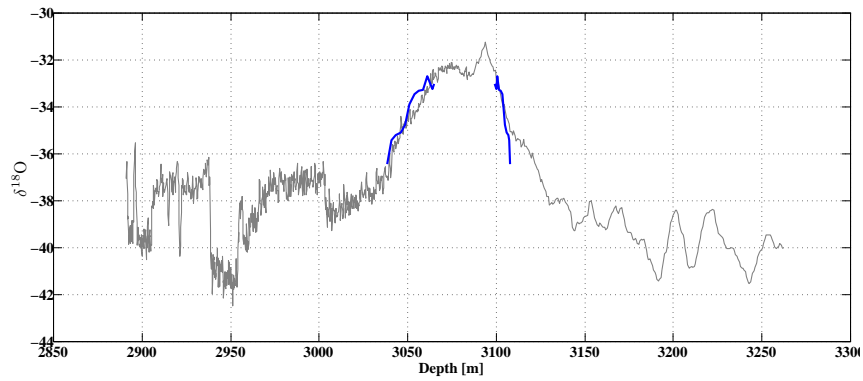
(b) Intervals selection in the ~ 2210 - 2430 m range.

Figure 5.6: NEEM record. The disturbed section is shown in the upper panel. Only a specific range is selected for the simulations. Below ~ 2430 m depth, the ice is assumed to be older with respect to the Eemian period.

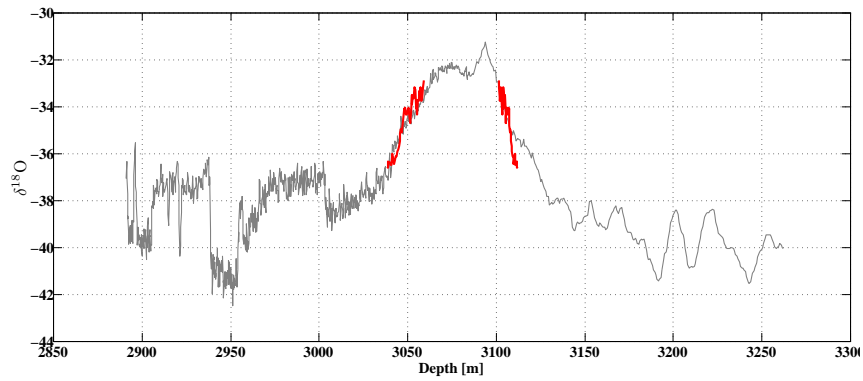
algorithm. The black dots indicate where the NEEM data series was divided; the coloured intervals (blue, red and green) are the interesting features, whose best match are plotted in fig 5.7 together with the alignment of their inverted profiles. Table 5.2 summarizes the boundaries of each interval as well as the scale and translation factors applied by *Match* for both orientations (shown by the arrows in the table). From fig 5.7a and 5.7b, it can be seen that the red and blue intervals match the same section of the reference profile, in whichever direction. This result supports the hypothesis suggested above. Fig 5.7c shows the alignment of the last interval. Since it matches precisely the same area of the gray function, the two representations are plotted in two shades of green for better visibility.

The simulation suggests different possible reconstructions, arising from the different order in which to position the coloured intervals. From a computational point of view they are all equally plausible. As suggested before, the red and blue sections might contain ice with the same age, either corresponding to (1) termination II (the ending of the penultimate glacial) or (2) to the cooling which led to the last glaciation. Another hypothesis would be the red and blue sections spanning respectively period (1) and (2), or viceversa. In all these possible reconstructions, the green interval would fit the same section, visible in fig 5.7c. In fact, whichever direction it is matched to the reference profile, the scaling and translation applied are comparable. This is not surprising as the corresponding ice is characterized by the least negative $\delta^{18}\text{O}$ ratio, with comparable values to the reference function. However, at a closer look, the straight profile (light green) matches more closely the reference record. The visual alignment, in this case, is remarkable.

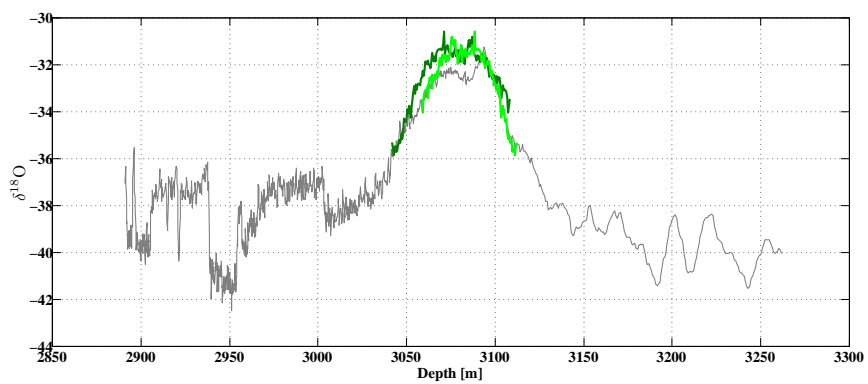
It should be noted that if the two gray intervals in fig 5.6b, following respectively the red and blue intervals, were added to the latter ones, the resulting match of these two sections (not shown) would be the same.



(a)



(b)



(c)

Figure 5.7: Alignments of the three intervals selected in the disturbed NEEM section. Both orientations are shown. In panel (c), two shades of green are used to better visualize the superposing lines.

GISP2 and GRIP

The work in this thesis was focused on the NEEM record. Nevertheless, the approach, as well as the single routines developed during the project, is quite general. Thus, it is very interesting to apply the method to the Summit cores, whose stratigraphy is also disturbed across MIS-5, and check whether some common features arise among the three records. However, the size of the disturbances at GRIP and GISP2 is very small, typically a few meters. This affects the *Match* algorithm, because the shorter the section to align to the reference function, the easier is to fit it somewhere. The application of the method on these records is therefore less reliable than at NEEM. Nevertheless, some interesting features can be highlighted. The GISP2 data section used in the simulation covers the section from 2750m depth to bedrock. Stable isotopes values typical of glacial ice can be seen between ~ 2900 - 2950 m depth, but at this site it is less clear whether deeper ice still belongs to MIS-5 or not. According to Suwa et al. (2006), the age of the ice in the ~ 2950 - 3000 m range mostly corresponds to the Eemian period, with some samples dated in MIS-6 and MIS-7.

However, this section is characterized by fluctuations in $\delta^{18}\text{O}$ values with both high amplitude and frequency, which prevented to select an interval to match to the reference function.

Three intervals were selected, shown in red, blue and green in fig 5.8. The sections







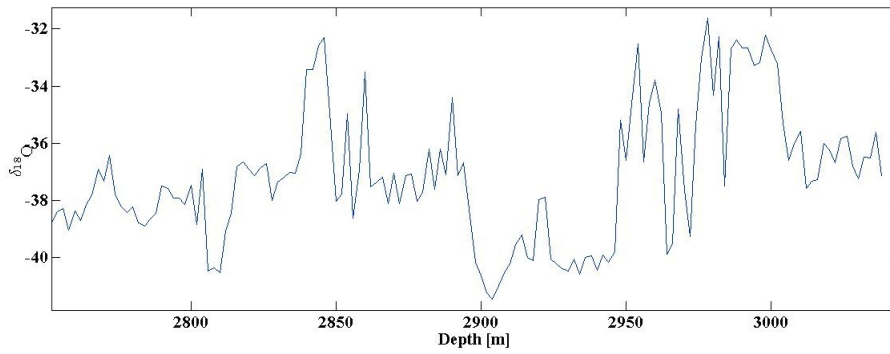
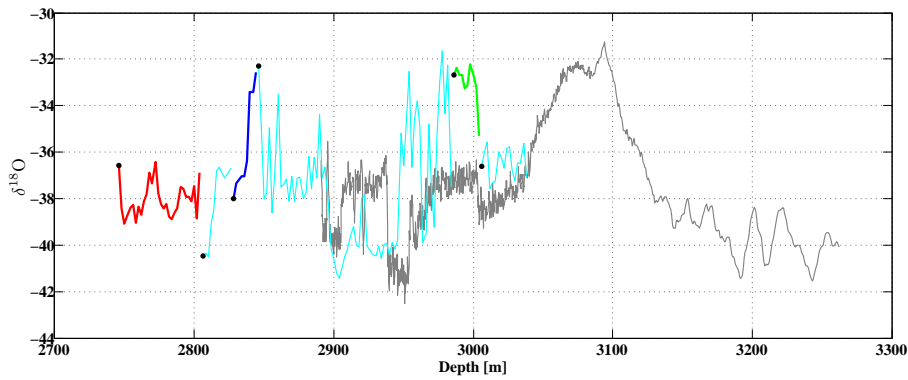
	\mathbf{x}_i	\mathbf{x}_f	\mathbf{s}	\mathbf{dx}
	2746.00	2804.00	0.23	3130.06
	2746.00	2804.00	0.51	3001.67
	2828.00	2844.00	2.47	3092.17
	2828.00	2844.00	2.14	3017.94
	2986.00	3004.00	2.47	3048.45
	2986.00	3004.00	0.20	3098.13

Table 5.3: GISP2. Boundaries (first two columns) of the selected intervals.



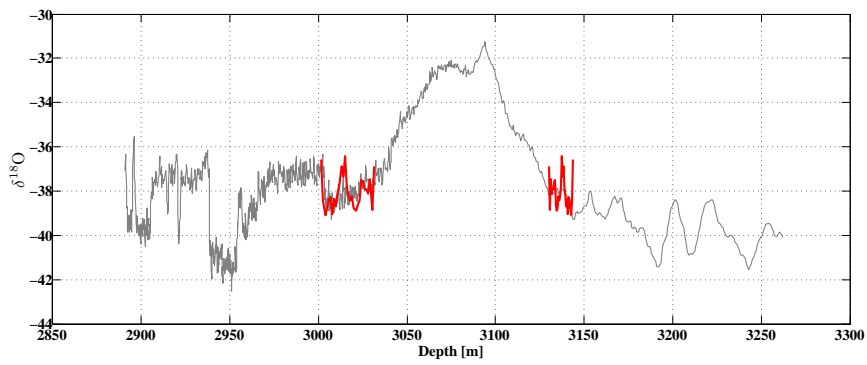
(a) Disturbed GISP2 section



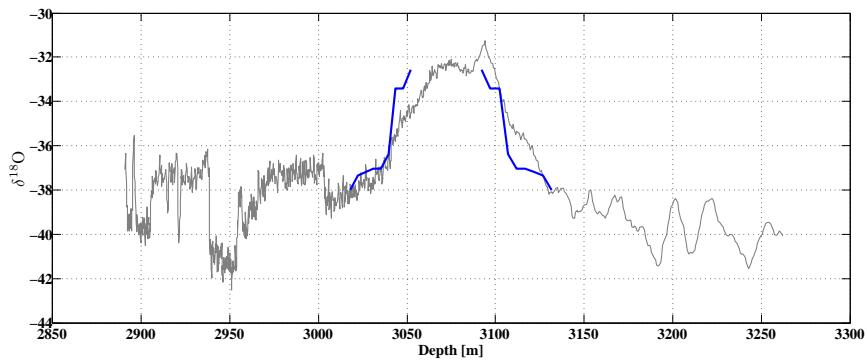
(b) Intervals selected for the comparisons (blue, red and green).

Figure 5.8: GISP2 record. The disturbed section is shown in the upper panel. The cyan blue line indicates the sections of ice not used in the simulation.

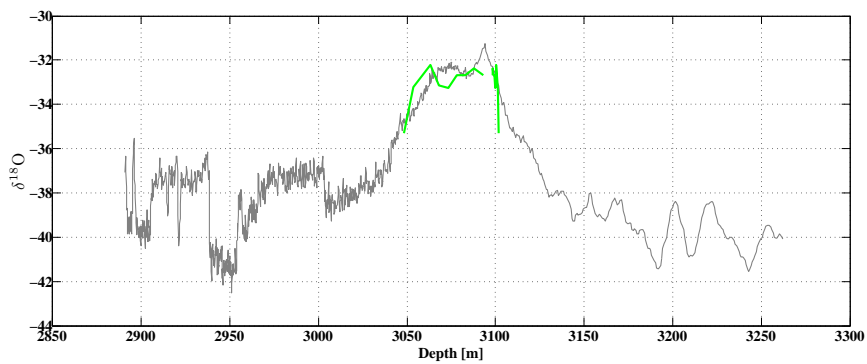
in cyan blue were not used for the simulation. The result is shown in fig 5.9. As mentioned before, these comparisons are less reliable than the NEEM results.



(a)



(b)



(c)

Figure 5.9: Alignments of the three intervals selected in the disturbed GISP2 section. Both orientations are shown.

With GRIP data, the method was applied to the ~ 2750 - 2900 m range. In fig 5.10, the interesting intervals are highlighted in different colors. The cyan blue line once more indicates the sections which were not matched to the gray reference profile.

As it was the case at the GISP2 site, also at GRIP the size of the foldings is quite

	x_i	x_f	s	dx
	2750.00	2758.25	0.98	3001.75
	2750.00	2758.25	3.61	3119.89
	2758.80	2786.30	0.44	3011.07
	2758.80	2786.30	1.65	3118.80
	2786.85	2795.65	0.22	3049.64
	2786.85	2795.65	2.80	3036.54
	2796.20	2807.20	3.78	3025.52
	2796.20	2807.20	2.71	3097.89
	2813.80	2834.70	0.33	3035.90
	2813.80	2834.70	2.06	3099.24
	2847.90	2869.35	3.29	3017.40
	2847.90	2869.35	1.65	3094.70

Table 5.4: GRIP. Boundaries (first two columns) of the selected intervals.

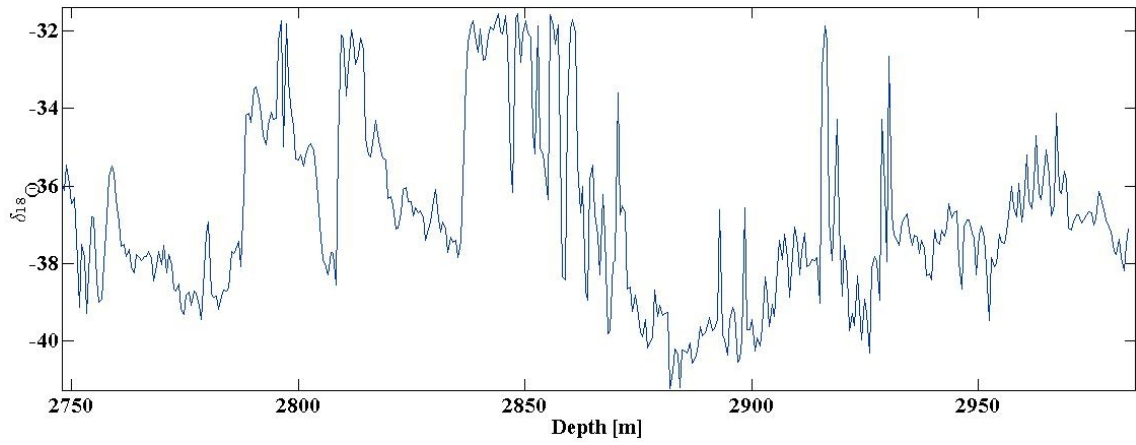
small with respect to NEEM. Variability in the stable isotopes profile is very pronounced, mostly in the dark blue section where changes are as big as 6‰.

The green and blue intervals (both light and dark shades), might represent both termination II or the beginning of the last glacial, depending on the direction. As show in fig 5.11, they actually fit these two temporal domains. However, they tend to look less convincing than at NEEM. The light blue function, for example, did not result in any meaningful match when inverted and only the original direction is shown in fig 5.10c. On the other hand, a particularly nice fit is estimated for the orange interval (inverted), positioned at the onset of the deglaciation. However, it must be noted that another work (Suwa et al., 2006) placed the ice at the corresponding depth at

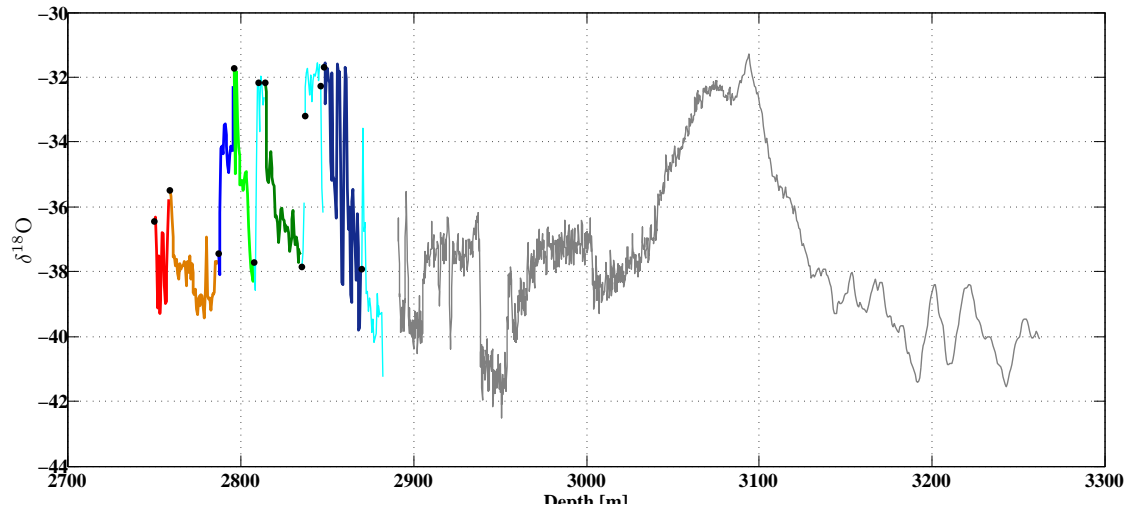
the end of MIS-5.

Finally, an interesting match is shown in fig 5.10f. Despite the highest variability pattern with respect to all the other intervals, the dark blue section is best fit at the end of the penultimate glacial as well.

In conclusion, a profile common to all the three records was not highlighted. This is due mostly to the high variability present at the Summit cores, which both complicates the use of the approach here developed and limits the reliability of the results. Nevertheless, some specific interesting features were noted, mostly in the NEEM record where some possible reconstructions were selected.



(a) Disturbed GRIP section



(b) Selected intervals for the comparisons are shown in different colors.

Figure 5.10: GRIP record. The disturbed section is shown in the upper panel. Only a specific range is selected for the simulations. Data below $\sim 2780\text{m}$ depth were not included in the simulations. The cyan blue line indicates the sections of ice not used in the simulation.

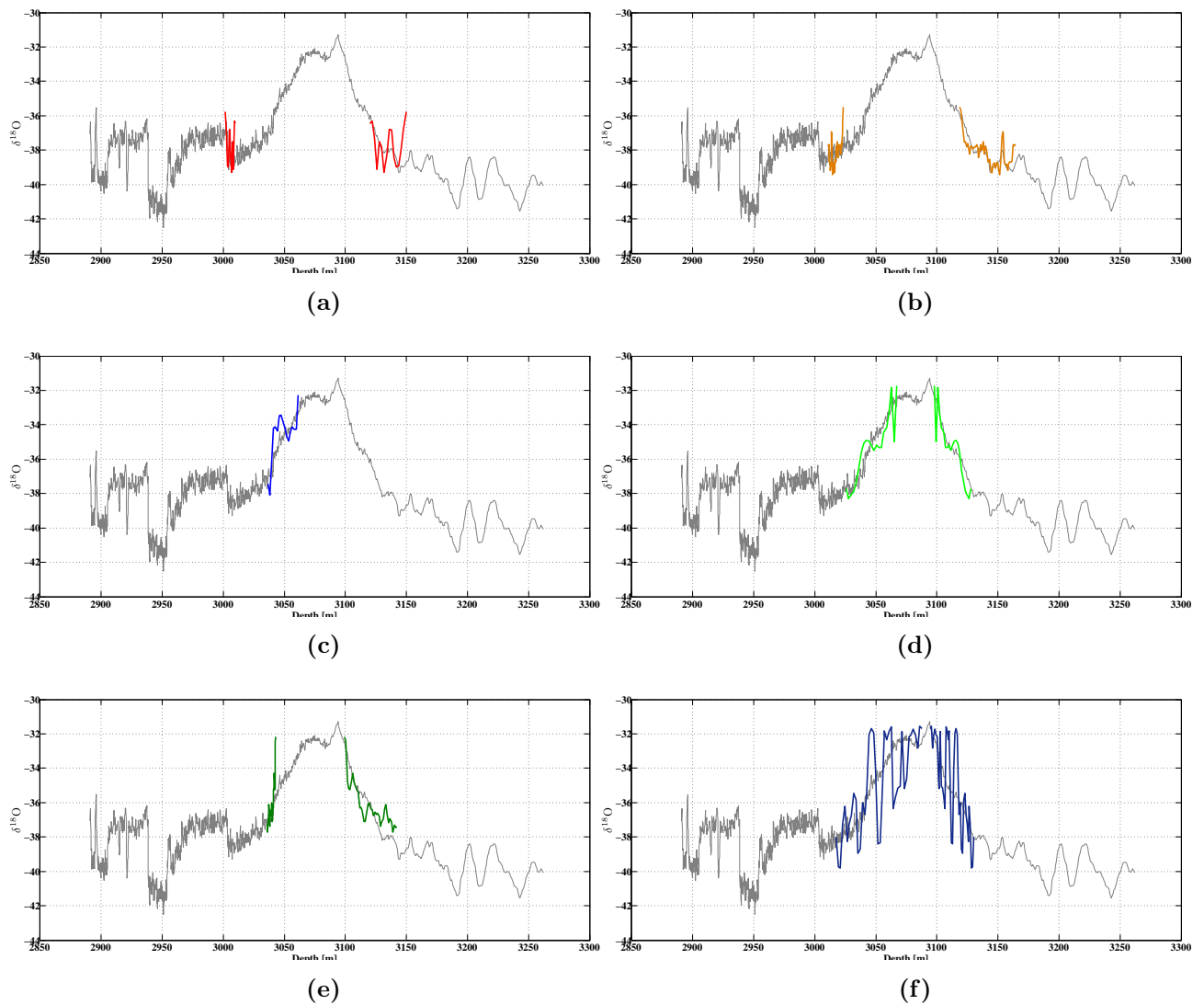


Figure 5.11: Alignments of the six intervals selected in the disturbed GRIP section. Both orientations are shown.

Chapter 6

Conclusions and discussions

This thesis dealt with the challenging task of reconstructing the correct chronology of the Eemian period (~ 115 - 130 Kyr BP) at NEEM. The method developed was then applied to the Summit cores as well, in order to check whether common features could arise. The motivations to the project are based on the importance of understanding how the penultimate interglacial began, developed and ended, with as much detail as possible. In fact, model projections of future climates predict similar temperatures to the Eemian period by 2100.

The approach of this work is based on a so called "exhaustive search" method. The disturbed data sections were split into intervals and possible candidate solutions were generated by the consecutive use of three operations: the (1) removal and (2) depth reversal of one or more intervals, plus the (3) exchange of two any intervals. Each configuration was then compared to a reference Eemian profile. Such function was obtained by the combination of real data from NGRIP until available (~ 123 Kyr BP), plus a synthetic reconstruction of Greenland variability based on an application of the thermal bipolar seesaw model (Barker et al., 2011).

The comparisons were performed by a dedicated routine (*Match*) at the core of

the whole method. This algorithm estimates the translation and scaling best aligning two given input functions. The power of such routine lies in its generality, as it is not strictly related to ice core data. Its application to NEEM undisturbed data ($\sim 1780\text{-}2200\text{m}$ depth) successfully aligned the section to the NGRIP record in about one minute run.

One current limit of *Match* is to not allow non-uniform, i.e. multiple, scalings. The algorithm could be substantially improved by this option. In fact, the process of aligning two functions whose different sections are rescaled with arbitrary factors would become fully automatic.

Another important improvement would be the introduction of a normalization process before the application of the actual routine. In this way, comparisons across different kind of data sets might be performed as well. Such a normalization should transfer the data values between zero and one, leaving intact the local differences between the minima and maxima of the record, i.e. preserving the main shape of the data series. In principle, such a process is not difficult, but issues may arise. For example, in the case the amplitude of response between the two records differed by a non-uniform offset, the algorithm would probably fail, as it is based on squared differences.

The whole method was then successfully tested on synthetic disturbed data series, generated out of the NGRIP record. The corrupted versions were created using the same operations described above, plus the application of an arbitrary but uniform scaling.

Once created, they were given as input to the *Main* program. Several simulations were performed, subsequently setting the breakpoints at increasing distance from the original position. Comparisons were done using the original NGRIP record as the reference profile. The original data sequence was successfully identified in almost all simulations, despite the offset applied to the breakpoints.

A fully automated way of identifying the best solution was not achieved and eventu-

ally a manual control had to be performed. Nevertheless, this operation was required only after the selection of a few candidate solutions out of the tens generated by the program.

At last, the *Main* program was applied to the disturbed data sections of the NEEM, GISP2 and GRIP records. Since *Match* did not estimate non-uniform scaling, the generation of candidate solutions by swap of the intervals was inhibited by avoiding the call of *Interchange* in *Operations*. Thus, the intervals in which the sections were split, together with their inverted versions, could be separately matched to the reference profile. The position of the breakpoints in the original data remained somewhat arbitrary. Their location was set by trying to highlight some possible features in the corrupted sections of ice, such as possible fragments' repetitions or inversions.

Eventually, some tentative reconstructions were proposed for the NEEM record. Two rather large ($\sim 50\text{m}$ and $\sim 100\text{m}$) sections of ice might belong to the same age and correspond to the beginning of the last glacial period (if inverted) or termination II. The application of the method to the Summit cores gave less robust results. In fact, the output was less reliable because of the considerably smaller size of the disturbances with respect to the NEEM site.

A profile common to the three records was not achieved at last. Nevertheless, possible reconstructions were proposed for the NEEM records and represent a first tentative of constructing a chronologically consistent section of the deepest part of the record. Moreover, the further development of the *Match* algorithm might open the way on comparing and aligning data sets from different types of records.

Bibliography

S. Anandakrishnan, R. B. Alley, and E. D. Waddington. Sensitivity of the Ice-Divide Position in Greenland to Climate Change. *Geophysical Research Letters*, 21(6):441–444, 1994.

Katrine K Andersen, Anders Svensson, Sigfus J Johnsen, Sune O Rasmussen, Matthias Bigler, Regine Ro, Urs Ruth, and Marie-louise Siggaard-andersen. The Greenland Ice Core Chronology 2005. *Quaternary Science Reviews*, pages 1–12, 2006.

S. Barker, G. Knorr, R. L. Edwards, F. Parrenin, A. E. Putnam, L. C. Skinner, E. Wolff, and M. Ziegler. 800,000 Years of Abrupt Climate Variability. *Scienceexpress*, 10, 2011.

R. S. Bradley. Paleoclimatology. Reconstructing Climates of the Quaternary, 2nd ed. *International Geophysics Series*, 64, 1999.

W S Broecker. Paleocean circulation during the Last Deglaciation: A bipolar seesaw? *Paleoceanography*, 13(2):119–121, 1998.

Jerome Chappellaz, Thomas Blunier, and Sophie Kints. Changes in the atmospheric CH₄ gradient between Greenland and Atarctica during the Holocene. 1997.

The Greenland Summit Ice Cores. The Greenland Summit Ice Cores CD-ROM. Available from the National Snow and Ice Data Center, University of Colorado at

- Boulder, and the World Data Center-A for Paleoclimatology, National Geophysical Data Center, Boulder, Colorado. *Journal of Geophysical Research*, 1997.
- Dorthe Dahl-Jensen, Niels Gundestrup, S. Prasad Gogineni, and Heinz Miller. Basal melt at NorthGRIP modeled from borehole, ice-core and radio-echo sounder observations. *Annals of Glaciology*, 37(1):207–212, 2003.
- W Dansgaard, S J Johnsen, H B Clausen, D Dahl-Jensen, N S Gundestrup, C U Hammer, C S Hvidberg, J P Steffensen, A E Sveinbjornsdottir, J Jouzel, and G Bond. Evidence for general instability of past climate from a 250-kyr ice-core record. *Nature*, 364(6434):218–220, 1993.
- GRIPmembers, M. Anklin, J. M. Barnola, J. Beer, J. Chgappellaz, H. B. Clausen, D. Dahl-Jensen, W. Dansgaard, M. De Angelis, R. J. Delmas, P. Duval, M. Fratta, A. Fuchs, K. Fuhrer, N. Gundestrup, C. Hammer, P. Iversen, S. Johnsen, J. Jouzel, J. Kipfstuhl, M. Legrand, C. Lorius, V. Maggi, H. Miller, J. C. Moore, H. Oeschger, G. Orombelli, D. A. Peel, Raisbeck G., D. Raynaud, C. Schott-Hvidberg, J. Schwander, H. Shojy, R. Souchez, B. Stauffer, J. P. Steffensen, M. Stievenard, A. Sveinbjornsdottir, T. Thorsteinsson, and E. W. Wolff. Climate instability during the last interglacial period recorded in the GRIP ice core. *Nature*, 364:203–207, 1993.
- P. M. Grootes, M. Stulver, J. White, S. Johnsen, and J. Jouzel. Comparison of oxygen isotope records fomr the GISP2 and GRIP Greenland ice cores. *Nature*, 366:552–554, 1993.
- AR4 IPCC. Climate Change 2007: The Physical Science Basis, Contribution of Working Group I to the Fourth Assessment Report of the Intergovernmental Panel on Climate Change [Solomon, S. and Qin, D. and Manning, M. and Chen, Z. and Marquis, M. and Averyt, K.B. and Tignor, M. and Miller, H.L., eds.]. *Cambridge University Press*, 2007.

- H Paul Jacobson and Edwin D Waddington. Recumbent folding in ice sheets : a core-referential study. *Journal Of Glaciology*, 50(168), 2004.
- J Jouzel, V Masson-Delmotte, O Cattani, G Dreyfus, S Falourd, G Hoffmann, B Minster, J Nouet, J M Barnola, J Chappellaz, H Fischer, J C Gallet, S Johnsen, M Leuenberger, L Loulergue, Luethi, H Oerter, F Parrenin, G Raisbeck, D Raynaud, A Schilt, J Schwander, E Selmo, R Souchez, R Spahni, B Stauffer, J P Steffensen, B Stenni, T F Stocker, J L Tison, M Werner, and E W Wolff. Orbital and Millennial Antarctic Climate Variability over the Past 800,000 Years. *Science*, 317, 2007.
- Jean Jouzel, Randal D. Koster, Robert J. Suozzo, and Gary L. Russel. Stable water isotopes behavior during the last glacial maximum: a general circulation model analysis. *Journal of Geophysical Research*, 99(D12):25,791–25,801, 1994.
- Peter G Knight, David E Sugden, and Christopher D. Minty. Ice flow around large obstacles as indicated by basal ice exposed at the margin of the Greenland ice sheet. *Journal of Geophysical Research*, 40(135), 1994.
- Amaelle Landais, Jerome Chappellaz, Marc Delmotte, Jean Jouzel, Thomas Blunier, Christine Bourg, Nicolas Caillon, Stephane Cherrier, Bruno Malaize, Valerie Masson-Delmotte, Dominique Raynaud, Jakob Schwander, and Jørgen Peder Steffensen. A tentative reconstruction of the last interglacial and glacial inception in Greenland based on new gas measurements in the Greenland Ice Core Project (GRIP) ice core. *Journal of Geophysical Research*, 108, 2003.
- C. Lang, M. Leuenberger, J. Schwander, and S. Johnsen. 16[±]°C Rapid Temperature Variation in Central Greenland 70,000 Years Ago. *Science*, 286(5441):934–937, 1999.
- Shawn J Marshall and Kurt M Cuffey. Peregrinations of the Greenland Ice Sheet divide in the last glacial cycle : implications for central Greenland ice cores. *Earth and Planetary Science Letters*, 179:73–90, 2000.

NEEM members. Paper in preparation.

NGRIPmembers, K K Andersen, N Azuma, J-M Barnola, M Bigler, P Biscaye, N Caillon, J Chappellaz, H B Clausen, D Dahl-Jensen, H Fischer, J Flückiger, D Fritzsche, Y Fujii, K Goto-Azuma, K Grønvold, N S Gundestrup, M Hansson, C Huber, C S Hvidberg, S J Johnsen, U Jonsell, J Jouzel, S Kipfstuhl, A Landais, M Leuenberger, R Lorrain, V Masson-Delmotte, H Miller, H Motoyama, H Narita, T Popp, S O Rasmussen, D Raynaud, R Rothlisberger, U Ruth, D Samyn, J Schwander, H Shoji, M-L Siggard-Andersen, J P Steffensen, T Stocker, a E Sveinbjörnsdóttir, A Svensson, M Takata, J-L Tison, Th Thorsteinsson, O Watanabe, F Wilhelms, and J W C White. High-resolution record of Northern Hemisphere climate extending into the last interglacial period. *Nature*, 431(7005):147–51, 2004.

Uwe Nixdorf and Fidan Goktas. Spatial depth distribution of the subglacial bed and internal layers in the ice around NGRIP, Greenland, derived with airborne RES. *Journal of Applied Geophysics*, 47:175–182, 2001.

S. O. Rasmussen, K. K. Andersen, a. M. Svensson, J. P. Steffensen, B. M. Vinther, H. B. Clausen, M.-L. Siggaard-Andersen, S. J. Johnsen, L. B. Larsen, D. Dahl-Jensen, M. Bigler, R. Röthlisberger, H. Fischer, K. Goto-Azuma, M. E. Hansson, and U. Ruth. A new Greenland ice core chronology for the last glacial termination. *Journal of Geophysical Research*, 111(D06102), 2006.

C. F. Raymond. DEFORMATION IN THE VICINITY OF ICE DIVIDES. *Journal of Glaciology*, 29(103):357–373, 1983.

M. Siddall, T. F. Stocker, T. Blunier, R. Spahni, J. F. McManus, and E. Bard. Using a maximum simplicity paleoclimate model to simulate millennial variability during the last four glacial periods. *Quaternary Science Reviews*, 25:3185–3197, 2006.

T. Stocker and S. Johnsen. A minimum thermodynamic model for the bipolar seesaw. *Paleoceanography*, 18, 2003.

- R. B. Stothers. The Great Tambora Eruption in 1815 and Its Aftermath. *Science*, 224(4654):1191–1198, 1984.
- Makoto Suwa, Joseph C. von Fischer, Michael L. Bender, Amaelle Landais, and Edward J. Brook. Chronology reconstruction for the disturbed bottom section of the GISP2 and the GRIP ice cores: Implications for Termination II in Greenland. *Journal of Geophysical Research*, 111(D02101):1–12, 2006.
- a. Svensson, K. K. Andersen, M. Bigler, H. B. Clausen, D. Dahl-Jensen, S. M. Davies, S. J. Johnsen, R. Muscheler, F. Parrenin, S. O. Rasmussen, R. Röthlisberger, I. Seierstad, J. P. Steffensen, and B. M. Vinther. A 60 000 year Greenland stratigraphic ice core chronology. *Climate of the Past*, 4(1):47–57, 2008.
- Elizabeth R Thomas, Eric W Wolff, Robert Mulvaney, Sigfus J Johnsen, Jorgen P Steffensen, and Carol Arrowsmith. Anatomy of a Dansgaard-Oeschger warming transition : High-resolution analysis of the North Greenland Ice Core Project ice core. *Journal of Geophysical Research*, 114(D08102):1–9, 2009.
- David G Vaughan, Hugh F J Corr, Christopher S M Doake, and Ed D Waddington. Distortion of isochronous layers in ice revealed by ground-penetrating radar. *Nature*, 398:323–326, 1999.
- B. M. Vinther, H. B. Clausen, S. J. Johnsen, S. O. Rasmussen, K. K. Andersen, S. L. Buchardt, D. Dahl-Jensen, I. K. Seierstad, M.-L. Siggaard-Andersen, J. P. Steffensen, A. Svensson, J. Olsen, and J. Heinemeier. A synchronized dating of three Greenland ice cores throughout the Holocene. *Journal of Geophysical Research*, 111(D13102), 2006.
- E.W. Wolff, J. Chappellaz, T. Blunier, S.O. Rasmussen, and a. Svensson. Millennial-scale variability during the last glacial: The ice core record. *Quaternary Science Reviews*, 29(21-22):2828–2838, 2010.

Siavash Zokai and George Wolberg. Image Registration Using Log-Polar Mappings for Recovery of Large-Scale Similarity and Projective Transformations. *IEEE Transactions on image processing*, 14(10):1422–1434, 2005.